A COMPARISON OF MAGNETOELECTRIC TRANSDUCER DESIGNS FOR USE AS WIRELESS MAGNETIC POWER RECEIVERS IN BIOMEDICAL IMPLANT APPLICATIONS

by

Tyrel Rupp

A thesis submitted to the faculty of
The University of Utah
in partial fulfillment of the requirements for the degree of

Master of Science

Department of Mechanical Engineering

The University of Utah

May 2018

The University of Utah Graduate School

STATEMENT OF THESIS APPROVAL

The thesis of **Tyrel Christian Rupp**

has been approved by the following supervisory committee members:

Shad J. Roundy , Chair _____
Date Approved

Hanseup Kim , Member _____
Date Approved

Jiyoung Chang , Member _____
Date Approved

and by **Tim Ameel** , Chair of

the Department of **Mechanical Engineering**

and by David B. Kieda, Dean of The Graduate School.

ABSTRACT

Inherent in the nature of medical implant designs is the need to minimize their size and subsequent impact to their environment of use. Recently, many of the mechanisms used in implants have been constructed on the micro and even nano scales, however powering these devices still remains a challenge. One of the more elegant solutions to this issue would be to construct a microscale wireless power receiver (or transducer) to deliver the needed power. This work serves to compare the viability of two transducer designs as candidates for their use as such a receiver.

In particular the designs both use alternating magnetic fields as the power transmission medium and mechanically couple the magnetic and electric domains. The first design is a longitudinal (extension) mode magnetoelectric laminate comprised of magnetostrictive and piezoelectric layers. The second design is a symmetrically built mechano-magneto-electric transducer consisting of a piezoelectric bimorph with a permanent magnet mounted at its tip.

A lumped parameter model was developed for the bending design while an existing model of the longitudinal design was augmented so that the power output of each device could be predicted and compared. Additionally, these models were experimentally validated. A linear numerical optimization was then performed using the models. The optimization was constrained at 2 mm^3 maximum size as well as by IEEE and ICNIRP field restrictions to reflect the requirements of a medical implant.

The results of the optimization showed that a magnetoelectric laminate made of

Metglas and PZT layers delivered more power than that of a symmetric mechano-magnetoelectric transducer made of Brass, PZT and Neodymium. Under IEEE field restrictions this amounted to ~40 mW of power delivery compared to ~4 mW. Under the ICNIRP restrictions the corresponding power outputs are ~60 μW and ~26 μW respectively. These results indicate that a magnetoelectric laminate, particularly under IEEE conditions, is the more feasible of the two designs for powering microscale implants and efforts should be made to develop such a transducer.

This thesis is dedicated to Gloria Rupp for teaching me to love learning, to Wally Rupp for instilling in me the importance of hard work, and ultimately to the both of them for demonstrating to me what can come when these two passions are combined.

TABLE OF CONTENTS

LIST OF TABLES

Tables

LIST OF FIGURES

Figures

LIST OF SYMBOLS AND ABBREVIATIONS

FEM	Finite element model
ICNIRP	International Commission on Non-Ionizing Radiation Protection
IEEE	Institute of Electrical and Electronics Engineers
IMD	Implantable medical device
ME	Magnetoelectric
MME	Mechano-magnetoelectric
MS	Magnetostrictive
MPE	Maximum Permissible Exposure
PE	Piezoelectric
PM	Piezomagnetic
PVDF	Polyvinylidene fluoride
PZT	Lead zirconate titanate
RF	Radio frequency
WPT	Wireless power transfer
L-L	Longitudinal-Longitudinal
L-T	Longitudinal-Transverse
T-L	Transverse-Longitudinal
T-T	Transverse-Transvers
A_1	Total piezoelectric cross-sectional area
A_2	Total magnetostrictive cross-sectional area

α_{ME}	Magnetoelectric coefficient
b	Damping coefficient
β_p	Inverse dielectric constant of piezoelectric material
$\bar{\beta}_p$	Effective inverse dielectric constant of piezoelectric material
C_0	Clamped piezo electric capacitance
C_m	Mechanical capacitance or compliance
$d_{33,m}$	Piezomagnetic material coefficient (parallel to field)
ϵ_0	Vacuum permittivity
e_{33}	Effective piezoelectric stress constant
E_P	Piezoelectric modulus of elasticity
E_s	Substrate modulus of elasticity
$(EI)_c$	Composite flexural rigidity
$f(x)$	Objective Function
F_m	Equivalent force due to magnet moment
$g_{33,p}$	Piezoelectric voltage coefficient (parallel to poling)
$g_{31,p}$	Piezoelectric voltage coefficient (perpendicular to poling)
h	Magnet height
H	Magnetic field strength
H_p	Sinusoidal magnetic field magnitude
H_{DC}	Continuous (DC) magnetic field magnitude
J_r	Remnant magnetic polarization
K_3^T	Relative dielectric constant
K_0	Short-circuit stiffness

K_1	Optimal load stiffness
ΔK	Change in stiffness due to loading
l	Laminate length
l_{eff}	Effective beam length
l_0	Length from anchor to free edge
L	Beam length
L_0	Beam length to magnet
L_m	Magnet length
L_m	Mechanical inductance or inertia
M	Magnet mass
m	Effective mass
m_b	Beam mass
M_b	Moment due to magnet
M_1	Variable used for simplification
λ	Magnetostriction constant
n	Volumetric layer ratio
ω	Operating frequency
ω_s	Fundamental/natural frequency
ω_1	Loaded natural frequency
P	Power output
P_p	Peak power output
P_{AVG}	Average power output (from RMS voltage)
P_{AVG}^{opt}	Optimal average power

φ_m	Magnetoelectric coupling coefficient
φ_p	Piezoelectric coupling factor
Q_m	Effective laminate quality factor
Q_p	Power output quality factor
Q_{ms}	Magnetostrictive quality factor
Q_{pe}	Piezoelectric quality factor
ρ_{avg}	Average laminate density
ρ_M	Magnet density
ρ_{ms}	Magnetostrictive material density
ρ_{pe}	Piezoelectric material density
ρ_s	Substrate density
s_{33}^H	Elastic compliance of the MS material (parallel to field)
s_{33}^D	Elastic compliance of the PE material (parallel to poling)
s_{11}^D	Elastic compliance of the PE material (perpendicular to poling)
S_{sub}	Structural interface layer
σ_T	Max tensile stress
σ_B	Max bending stress
t_p	Piezoelectric layer thickness
t_m	Magnetostrictive layer thickness
t_s	Substrate thickness
t_t	Total Beam/Laminate Thickness
τ	Time constant
v	Magnetoelectric wave speed

V_m	Magnet volume
V_{ORMS}	Open circuit transducer Voltage (RMS)
V_s	Substrate volume
V_{PE}	Piezoelectric volume
w	Beam/laminate width
x	Input parameters
x_0	Initial guess
X_0	Variable used for simplification
Z_0	Characteristic mechanical impedance
Z_m	Mechanical impedance or damping

ACKNOWLEDGMENTS

I would like to thank all those who have helped make thesis come to reality. Firstly, gratitude goes to Binh Duc Truong for the contribution of his model as a foundation to this work. Next, I would like to thank my committee members Hanseup Kim and Jiyoung Chang for their guidance during my time at the University of Utah. I would also like to thank the National Science Foundation for funding this project. Great appreciation also goes to all members of the Integrated Self-powered Sensing Laboratory for their contributions and friendship. Finally, greatest thanks go to my advisor and committee chair, Dr. Shad Roundy, for his extreme patience, guidance, and contributions throughout this project and my graduate school experience.

CHAPTER 1

INTRODUCTION

The continuous improvement of Implantable Medical Devices (IMD) is driven largely by their proven usefulness in monitoring and augmenting the environment found within the human body. In the case of Type 1 diabetic patients, the ability to continuously monitor blood glucose levels provided by implanted probes has been shown to reduce time spent in hypoglycemia [1]. This mitigation of a potentially fatal condition common to diabetics is just one of many success stories for IMDs. Beyond real time monitoring, the ability to deliver targeted drug doses and treat neural disorders via neural prostheses are just a few of the treatment methods becoming more viable as implants continue to develop [2], [3]. Utilizing the same technology that brought about micro scale semiconductors, microfabrication techniques have been used to develop a wide array of micro sized architectures that could be tremendously useful as implants to the human body [4]. Along with the reduction in size of the operating mechanisms, significant effort has also been put into miniaturizing circuitry required to operate them [5]. As it stands, the limitation behind implementing these microsystems as IMDs is not so much the size of the sensing mechanism or its circuitry, but rather the size of system used to power it. To make microscale IMDs more viable, microscale power systems need to be developed.

1.1 Project Motivation

Currently the most common way to power IMDs is via a direct (wired) external source or a battery implanted along with the IMD. Another proposed method is to utilize a wireless power transfer (WPT) system that can pass power through flesh and bone to the interior of the human body. Direct power delivery is typically avoided where possible due to the limitations it causes in patient mobility as well as the increased medical risks associated with passing wires transcutaneously to the location of the implant. Batteries help mitigate the problems presented by the direct powering method, however they also come with their own pitfalls. In the best of cases, batteries have finite lifetimes and require periodic replacement. More commonly however, in terms of microscale systems, the sheer size of the batteries alone nullifies the gains made by miniaturizing the other components of an IMD.

In light of the concerns with the two previously discussed methods, a WPT system would appear to be the obvious solution but is not without its own set of difficulties. Acoustic WPT systems have been investigated, but are complicated by the inability to transmit through bone and the need for direct skin contact [6]. Similarly, Radio frequency (RF) methods are viable for larger applications, however as RF receivers are miniaturized their operating frequencies are driven to levels where tissue tends to absorb and attenuate the transmitted signal [7]. This attenuation is not only inefficient, it is potentially hazardous because of associated tissue heating. In light of these difficulties, it rapidly becomes apparent that further research into WPT systems is required to more fully tailor them to the constraints posed by the human body.

1.2 Project Goals

With the need for an improved WPT method for use in microscale IMDs demonstrated, the goal of this project is to evaluate the practicality of two magnetic field based methods of WPT as alternatives to RF, acoustic, and inductive coupling methods applied at microscale sizes. In particular these methods look at two different types of receiver structure designs, a magneto-electric laminate (ME) extensional mode transducer and a Mechano-Magneto-Electric (MME) bending mode transducer.

This goal will be accomplished by first experimentally validating two lumped parameter models representative of the structures in question with macro scale transducers. Next both models will be used to yield geometries optimized for maximum power output at microscale sizes. The optimization will be driven by both microscale manufacturing constraints as well as biological constraints.

Ultimately the main contribution of this project is to use macro sized structures and modeling to identify which of the two methods (ME or MME) is superior for use at microscale levels, long before any costly microfabrication has to be performed.

CHAPTER 2

A REVIEW OF MAGNETOELECTRIC TRANSDUCERS AND THEIR WPT APPLICATIONS

As early as the year 1900, Nikola Tesla was patenting technology related to wireless energy transfer, and by 1905 he was convinced of its potential to revolutionize the world [8], [9]. This effort demonstrated the model for all future wireless energy transfer research by showing the need for both a transmitter to send the power and a receiver to capture the power. Despite Tesla's enthusiasm, for many years research into wirelessly powering devices was largely dwarfed by research on wireless communication. In the case of transcutaneous wireless power transfer, the topic did not become active until the 1960's and even then was sparse for the next two decades [10]. Finally, the suggestion to use magnetoelectric (ME) transducers to power IMDs only has only come in the last two decades as feasibility of ME laminates for WPT has been shown [11].

2.1 Non Magnetoelectric based Wireless Power Transfer Systems

As was indicated previously, WPT research has typically been based around structures that employ either magnetic, RF, acoustic, or inductive coupling techniques. It should be noted that the research at hand focuses mainly on magnetic techniques. Correspondingly, a detailed literature review of the other three techniques was considered

to be superfluous. Rather, the rest of section 2.1 is a brief summary of how these methods compare when applied to IMDs. In terms of content, unless otherwise cited, this summary comes from an extensive review performed by Basaeri et al. [12].

2.1.1 Inductive Coupling based WPT

In terms of actually implementing WPT systems to power implants, those utilizing inductive coupling appear to be the most advanced, principally in the case of powering pacemakers. Recently Abiri et al. demonstrated functionality of a porcine implanted, commercial pacemaker (St. Jude Tendril SDX Model 1388T) powered wirelessly by an *ex vivo* inductively coupled system [13]. Fundamentally, inductive coupling utilizes a pair of coils or antennas which must be closely and well aligned to allow for the transfer of power. Subsequently the amount power transfer is highly dependent on the size, orientation, operating frequency of, and distance between the antennas [14]. Ultimately these dependencies make this form of WPT most viable for IMDs (such as a pacemaker) where the depth of the implant is relatively shallow and the alignment of the coils can be well controlled.

2.1.2 Acoustic based WPT

Acoustic WPT, like inductive power transfer, is very alignment dependent in that the receiver must be well aligned (i.e. precise depth and orientation) to adequately receive the ultrasound signals being transmitted. Furthermore, to send useful amounts of power, the transmission medium, typically water or tissue, needs to be consistent. Air gaps or solids such as bone quickly attenuate the transmission signal. In terms of implementation, acoustic transducer research hasn’t gone much beyond porcine tissue experiments [15].

Nevertheless, given the ability to be implanted deeper and operate at much lower frequencies than RF and inductive systems, acoustic WPT shows promise, notably for powering IMDs located abdominally.

2.1.3 Radio Frequency based WPT

Radio frequency based WPT systems, like the others discussed, have both pros and cons. Unlike acoustic and inductively coupled systems, alignment is not as critical because receivers do not need to be coupled to the transmitter. However, concerns arise with RF receivers as their size decreases. As receivers are miniaturized, efficiency drops precipitously and reduced antenna sizes lead to high operating frequencies. This leads to transmitters having to operate at levels of electromagnetic radiation that area considered dangerous for humans due to induced tissue heating. Just the same, research to mitigate these effects continues undeterred, as demonstrated by the recently designed RF-powered microscale neural implant radio built by Rajavi et al. [16].

2.2 Development of the Magnetoelectric Effect

The magnetoelectric (ME) effect fundamentally refers to any type of coupling between electric and magnetic fields found in matter [17]. The first work with such an effect was done by Röntgen in 1888 when he showed theoretically that by moving a dielectric material through an electric field it would become magnetized [18]. That same effect was not confirmed experimentally until 1960 when Dzyaloshinskii witnessed it in Cr_2O_3. Despite this breakthrough, subsequent research showed that at best the magneto electric coefficient (α_{ME}) for bulk materials such as Cr_2O_3 was very low, on the order of

100 mV/(cm·Oe) [19]. This along with other various complications, kept the materials from of much use in practical applications [17].

2.2.1 History of Magnetoelectric Composites

Before the ME effect was even observed in bulk materials, Tellegen suggested developing composites that demonstrated a cumulative ME effect [20]. The implication here is that by coupling two separate physical effects (piezoelectric (PE) and magnetostrictive (MS)) in two separate materials an equivalent ME effect could be obtained.

The more commonly utilized piezoelectric effect is witnessed in materials that couple mechanical strain to an induced electric field. Similarly, the magnetostrictive effect found in some materials couples mechanical strain to an induced magnetic field. By linking two such materials mechanically, the resulting pseudo ME effect can be demonstrated simply as [21]

$$\text{ME Effect} = \frac{\text{electrical}}{\text{mechanical}} \times \frac{\text{mechanical}}{\text{magnetic}} \tag{2.1}$$

where the mechanical components in essence cancel out. For almost three decades attempts to form such a composite involved variations on sintering together small grain or particulate mixtures of both types of materials, however none of these composites were shown to have ME coefficients much larger than those found in bulk ME materials [17].

In 1998 Shin et al. bypassed particulate composites and attempted a three-layer laminate composite approach where the MS material was sputtered as a thin film onto a

glass substrate which was then bonded onto a PE base. This design has become known in the literature as a unimorph and is shown in Figure 2.1. By applying a voltage to the PE, the bending strain induced into the MS material caused large changes to its magnetic properties [22].

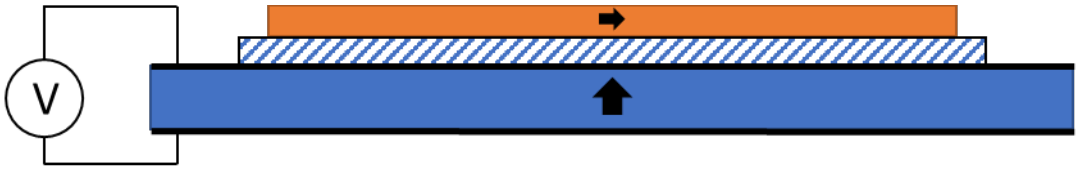

Figure 2.1: Magnetoelectric structure layout similar to that made by Shin et al. The MS material is and orientation is shown in orange, the PE material in blue, and the glass is in-between.

Building on the ME laminate approach taken by Shin et al., Ryu et al. developed another ME laminate using a sandwich design. This design used silver epoxy to bond a PZT-5A PE disk between two Terfenol-D MS disks. Measuring the α_{ME} under various magnetic field strengths yielded values up to 4.68 V/(cm·Oe) [23]. Not only was this an overwhelming improvement to the mV/(cm·Oe) level previously reported for particulate based ME composites, it brought the ME effect to a point of usefulness.

2.2.2 Development of Magnetostrictive Materials

Just as critical to ME laminate development was the materials involved. The work done by Ryu et al. relied upon a material, as indicated previously, known by the trade name “Terfenol-D.” As a rare earth alloy composed of Terbium, Dysprosium, and Iron, Terfenol-D is a direct product of extensive research done by the U.S. navy in the 1960s to find a material with what is now known as a “giant” magnetostrictive effect when placed

in a magnetic fields [24]. Terfenol has a saturation microstrain of 2500 ppm (μm/m). By comparison, cobalt and nickel have the largest known bulk material saturation microstrain on the order of 10 ppm, hence the term “giant” [25].

In the late 90s the U.S. Navy also discovered that Galfenol, an iron-gallium alloy, had high magnetostriction[26]. With a maximum saturation strain of 400 ppm, Galfenol is an attractive alternate to Terfenol-D because it costs about 80% less to manufacture and is significantly easier to machine[27]. A final MS material that should be mentioned and will be discussed more rigorously later in the body of this thesis is an amorphous metal known by its trade name as METGLAS (2605SA1). Although it does not have an exceptionally high maximum MS saturation strain (23 ppm), its high magnetic permeability allows for the maximum saturation to occur at much lower magnetic fields than most any other MS material[28], [29].

2.3 Review of Magnetoelectric Laminate Work

Following closely on the work done by Ryu et al., Dong et al. published a series of papers which have become seminal works for the design and modeling of sandwich, or extensional bimorph, ME transducer designs and configurations [30]. Initially, Ryu et al. only mathematically described the ME coefficient that they experimentally witnessed using static elastic constitutive equations [23]. The Dong et al. research recognized that fundamentally the ME effect would be more useful if it was understood under dynamic drive and utilized an equivalent circuit method to derive such a dynamic model for the bimorph transducer [31]–[33]. Furthermore, the work experimentally validated these models with devices built from PZT and Terfenol-D Plates [34]

2.3.1 Magnetoelectric Bimorph Designs

More explicitly, their work created model subsets for each of the four coupling orientation combinations possible for the PE and MS materials within the laminate structure. These configurations are compiled and shown in Figure 2.2 and indicate whether the PE and MS materials are poled longitudinally or transversely to the bimorph structure.

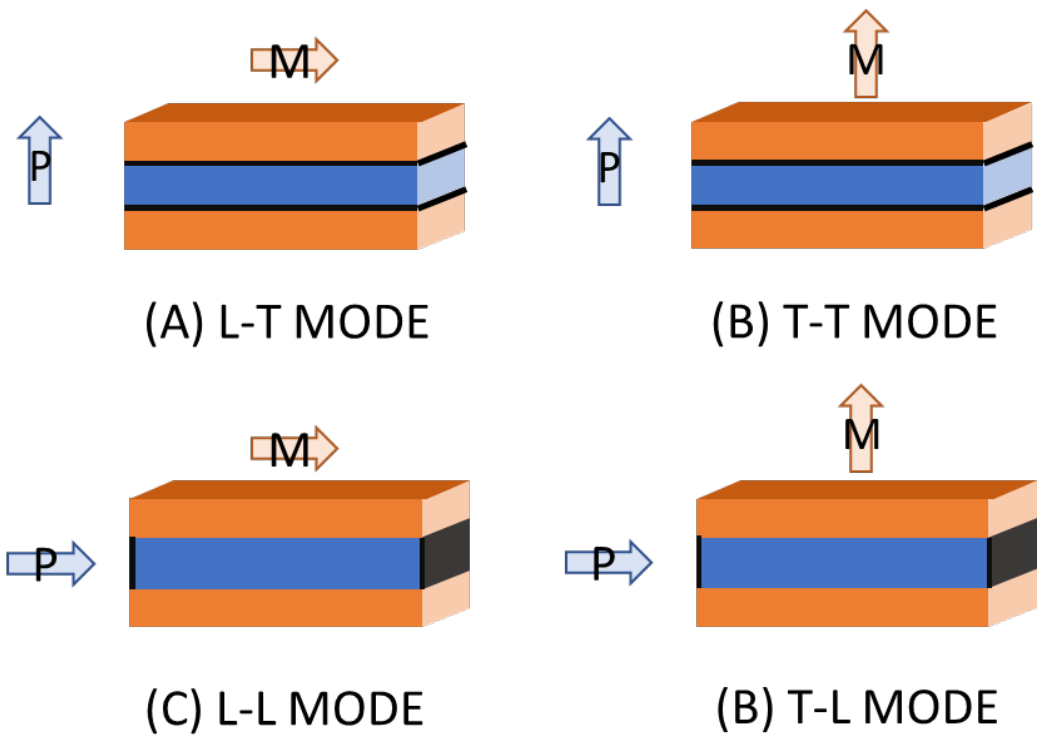

Figure 2.2: Four bimorph laminate orientation combinations. Orange indicates MS material, blue the PE material, and black the location of the PE poles. Additionally, the letters in the mode names, T for transverse and L for longitudinal, indicate the orientation of the MS material and PE material respectively. Compiled from [31]–[34].

Although a tremendous amount of work has gone into the extensional mode bimorph structures, many other laminate designs have been considered, not the least of which is the unimorph design that was used originally by [22]. Unlike the bimorph, the unimorph design is not a symmetric laminate which means that its first mode shape under magnetic drive is in bending rather than extension. This has been argued to be advantageous in that it has a lower natural frequency than the bimorph, however it remains for the efficiency of the two structure designs to be critically compared [30].

Beside the unimorph, a whole variety of other exotic designs exist or have been proposed for pseudo ME transducers. For the sake of this research most of the geometries add a level of complexity that is both prohibitive for modeling as well as manufacturing at the microscale [35]. However, there is one final design that requires mentioning.

2.4 Mechano-Magnetoelectric Design

Fundamentally, a magnetoelectric transducer is any device that takes energy from the magnetic domain to the electric domain and vice versa. Up to this point the transducers previously discussed fall into this category, as well as the category of pseudo ME material since they can be altered like a bulk material and still maintain their ME properties.

Recently another type of ME transducer, that is fundamentally not a pseudo ME material, has been proposed. This transducer operates by coupling the moment induced on ferromagnet by a magnetic field with a bending or cantilever PE beam. This is done by anchoring one end of the beam and by mounting the ferromagnet at the tip of the beam oriented perpendicular to the field [36]. To this point, the research done on such a device

has been for the purpose of energy scavenging and the corresponding models are found to be lacking. Nevertheless the design shows significant promise for WPT [36], [37].

Although fundamentally using the same designs of interest, publications have yet to use a consistent name for this geometry. As it such will be referred to in this work simply as a Mechano-Magnetoelectric or MME device.

2.5 Current applications of ME transducers

Originally the motivation behind the U.S. Navy to develop MS materials was for the use in sonar systems, however the progress made has ME applications a growing field of research [24].

2.5.1 ME Applications: Sensors and other electronic devices

The most notable application for magnetoelectric composites is in sensing AC and DC magnetic fields and for current sensing. Multiple designs have been suggested, demonstrated, and even patented that use thin film ME composites at micro and nanoscales [38], [39]. These designs are particularly useful for their extremely high sensitivities to changes in magnetic fields [40], [41]. In addition to sensing, there are also applications for ME composites as gyrators and transformers in microwave devices and as microactuators[42].

2.5.2 ME Applications: Medical uses

O'Handley et al. first suggested utilizing a ME bimorph for transcutaneous power transfer in 2008. Additionally, their research showed that in air a .1 cm^3 receiver could generate 2 mW at a distance of 3 cm from a transmitting solenoid[11]. Citing O'Handley

et al, Paluszek et al. make cases for how wireless endoscopy, brain imaging, and surgical tools might benefit from the use of ME based WPT[43]. Nonetheless, it would appear that with the exception of some finite element verification work, very little has been done to move the medical research forward[44].

Therefore, the intent of this research project is to move medical WPT research forward. This will be done by comparing optimal magnetoelectric traducer architectures that meet the constraints of medical usage.

CHAPTER 3

LUMPED ELEMENT MODELS FOR MAGNETOSTRICTIVE AND DOUBLE CANTELEVER TRANSDUCERS

As has been discussed, Dong et al. presented a lumped element, also known as an equivalent circuit, model to describe the performance of ME bimorphs across the magnetic, mechanical and electric domains [33]. This approach is not exclusive to bimorphs but is in fact a commonly used approach to model all types of vibrational energy harvesters, a category which the ME bimorph fundamentally falls into due to the vibrations induced by the MS material. Lumped element models are advantageous in that they typically yield analytical solutions which in turn yield physical insight and a foundation for preliminary design [45]. Subsequently the body of this research will utilize this modeling approach to describe the two ME transducer geometries being compared.

3.1 Lumped Parameter Power Model for ME bimorph

The first geometry of interest is that of the previously discussed ME bimorph. To simplify the modeling process, the well validated Dong et al. ME bimorph voltage model was used as the backbone of the power delivery model. The presentation of the model varies in the four initial papers published, however this work follows the nomenclature found in [31].” The most complete derivation can be found in [33].

3.1.1 Summary of the ME bimorph voltage model by Dong Et Al.

The longitudinal-longitudinal (L-L) oriented ME bimorph modeled by Dong et al. follows the design shown in Figure 3.1. This configuration allows the ends of the laminate to extend and compress along the length of the laminate. By examination one can see the neutral or nonmoving axis at the center of the laminate where the laminate would be fixed, as indicated by the anchor symbol.

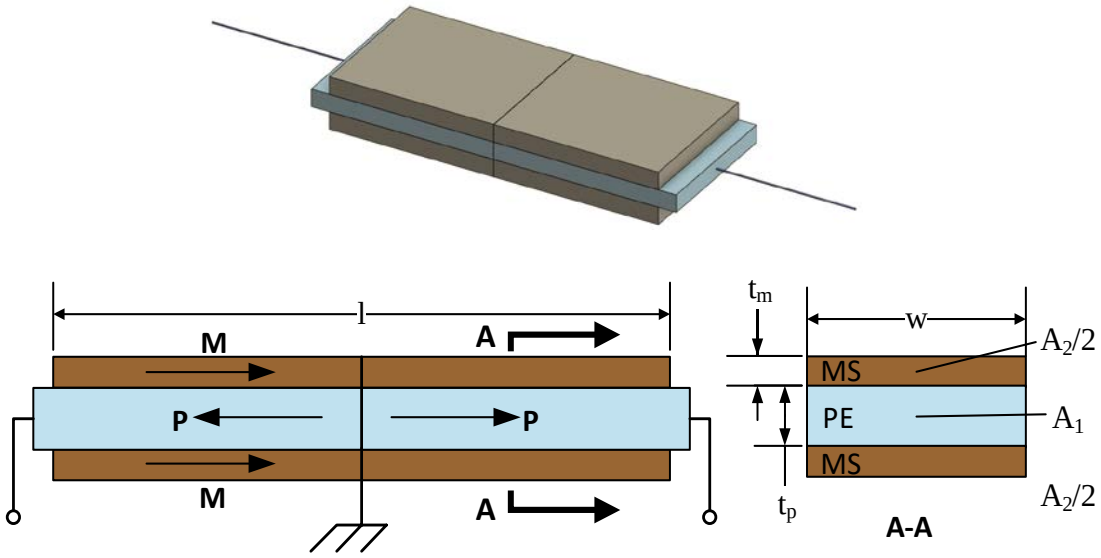

Figure 3.1: Geometry layout for L-L mode bimorph. Arrows M and P show the magnetization and polarization orientation. Adapted from [31], [33].

The corresponding lumped element model to that presented in Figure 3.1 is found in Figure 2.2. As shown by the figure, the MS transduction in the model is defined by the magnetoelectric coupling coefficient, φ_m, which is defined as

$$\varphi_m = \frac{A_2 d_{33,m}}{s_{33}^H} \left[\frac{N}{A/m}\right] \tag{3.1}$$

where A_2 is the total cross-sectional area of the MS layers, $d_{33,m}$ is the magneto-elastic or piezomagnetic (PM) coefficient in the longitudinal direction, and s_{33}^H is the elastic compliance of the MS material also in the longitudinal direction. When multiplied by the magnetic field level H, φ_m yields the force caused by the MS layer.

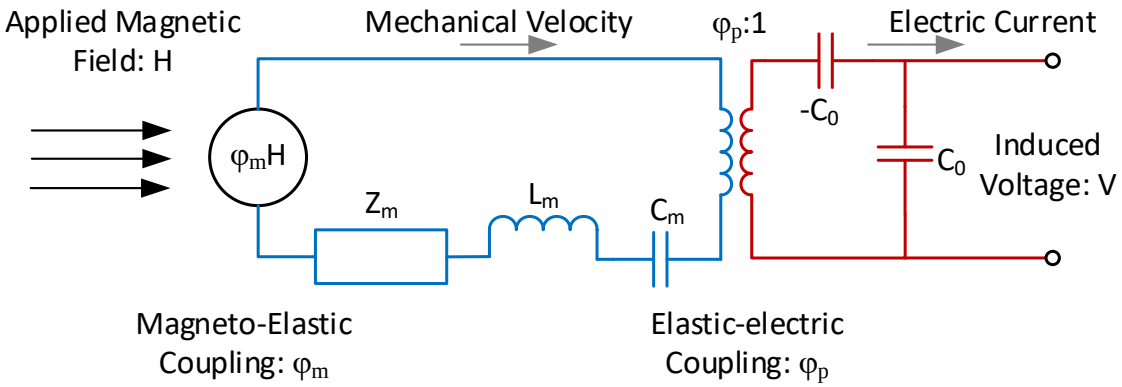

Figure 3.2: Lumped element equivalent circuit of L-L ME laminate. Adapted from [31].

Similarly, the PE transduction in the model is defined by the Elasto-Electric or Piezoelectric Coupling factor, φ_p which is defined as

$$\varphi_p = \frac{A_1 g_{33,p}}{l s_{33}^D \bar{\beta}_p} \left[\frac{N}{V}\right] \tag{3.2}$$

where A_1 is the cross section of the piezoelectric layer, and l is the length of laminate. Also $g_{33,p}$ is the longitudinal piezoelectric voltage coefficient, s_{33}^D is the longitudinal compliance and $\overline{\beta}_{33}$ is the inverse dielectric constant, all of which are material properties of the piezoelectric material. The piezoelectric coupling is modeled as a transformer in the LEM and relates the force caused by the MS layer to the voltage of the PE layer.

The electrical capacitance in the circuit, C_0 or clamped capacitance is defined as

$$C_0 = \frac{A_1}{l\,\overline{\beta}_p}\left[\frac{N}{V}\right] \tag{3.3}$$

and is caused by capacitance between piezoelectric material's poles. The value for $\overline{\beta}_{33}$, the effective inverse dielectric constant is calculated by

$$\overline{\beta}_p = \beta_p\left(1 + \frac{g_{33}^2}{s_{33}^D \beta_p}\right)\left[\frac{m}{F}\right] \tag{3.4}$$

The mechanical impedance (damping), Z_m, inductance (inertia), L_m, and capacitance (compliance), C_m are defined as

$$Z_m = \frac{\pi Z_0}{4Q_m}\left[\frac{kg}{s}\right] \tag{3.5}$$

$$L_m = \frac{\pi Z_0}{4\omega_s}\,[kg] \tag{3.6}$$

$$C_m = \frac{1}{\omega_s^2 L_m}\left[\frac{s^2}{kg}\right] \tag{3.7}$$

where Q_m is the effective quality factor for the laminate, ω_s is the fundamental frequency of the laminate and Z_0 is the characteristic mechanical impedance of the laminate in the extensional mode. These remaining lumped mechanical parameters were derived by Dong et al. by solving the second order equation of motion for the system. The results of this derivation are summarized in Table 3.1.

By performing circuit analysis in the frequency domain on the equivalent circuit in Figure 3.2. the effective ME coefficient, accounting for the dynamics of the structure is derived as

$$\alpha_{me} = \frac{\partial V_{me}}{\partial H} = \left| \beta \frac{\varphi_p}{j\omega C_0} \frac{\varphi_m}{Z_m + j\omega L_m + \frac{1}{j\omega C_m}} \right| \left[\frac{V}{A/m}\right] \tag{3.8}$$

where $\beta \leq 1$ is the ME bias factor, which will be discussed in more depth in the following section, and ω is the operating frequency of the magnetic field H. One will note that the φ_p parameter is not squared as it is believed to be an error in the reporting of the original model.

3.1.2 Limitations of Dong et al. model

With any lumped parameter model, it is critical to understand under what conditions the model is applicable, which in turn requires an understanding of the assumptions made therein. In the case of the Dong et al. model, a few of the assumptions made are particularly important.

Table 3.1: Lumped parameter equations for L-L ME laminate. Adapted from [33].

Lumped Parameter Variable	**Constitutive Equation**
Characteristic Mechanical Impedance, Z_0	$Z_0 = \rho_{avg} v * (A_1 + A_2) \left[\frac{kg}{s}\right]$
Average Laminate Density, ρ_{avg}	$\rho_{avg} = \frac{\rho_{ms} A_2 + \rho_{me} A_1}{A_1 + A_2} \left[\frac{kg}{m^3}\right]$
Magnetoelectric Wave Speed, v	$v = \sqrt{\frac{n}{s_{33}^H} + \frac{(1-n)}{s_{33}^D}} \left[\frac{m}{s}\right]$
Volumetric Layer Ratio, n	$n = \frac{A_2}{A_2 + A_1}$
Fundamental Frequency, ω_s	$\omega_s = \frac{\pi v}{l} \left[\frac{rad}{s}\right]$
Effective Laminate Quality Factor, Q_m	$Q_m = \left(\frac{n}{Q_{ms}} + \frac{1-n}{Q_{me}}\right)^{-1}$
Magnetostrictive Material Density, ρ_{ms}	Material Property
Piezoelectric Material Density, ρ_{pe}	Material Property
Magnetostrictive Quality Factor, Q_{ms}	Material Property
Piezoelectric Quality Factor, Q_{pe}	Material Property

Mechanically the model makes a very unconservative assumption in that it assumes that there is perfect and uniform strain transfer from the MS layer into to the PE layer. This implies that the interface joint between the laminates is taken as infinitely stiff and that there is no strain gradient through the thickness of the laminate. For the first implication, this means that if there is some sort of interface between the laminates such as a compliant epoxy matrix, the model will over predict the ME coefficient and reduce the effective laminate quality factor. A common mitigation approach to this is to experimentally measure laminate's quality factor and use the result to tune the model.

As to the uniform strain assumption, the accuracy varies with the laminate geometry as well as material properties. Fundamentally, the longer and thinner the laminate the more accurate this assumption will be, however the relative layer thickness, as defined by the volumetric layer ratio, n, also influence the strain uniformity which makes it difficult to make a global rule for what point the model geometry is no longer valid. To date the literature doesn't report a number for the length to total thickness ratio of the laminate, however structures with $l: \left(t_p + 2t_m\right) \geq 5$ have been used to experimentally validate the dong model [29], [34].

Another item to be cautious of is the linear assumption for material properties. For most properties, such as compliance, it is sufficient to say that for the operating range experienced, the property is sufficiently linear. But in the case of magnetostriction, making the appropriate linear assumption takes a bit more work. The piezomagnetic coefficient is defined as

$$d_{33,m} = \frac{d\lambda}{dH} \tag{3.9}$$

where λ is the magnetostriction of a given MS material [29]. Simply put the PM coefficient is the rate of magnetostriction change to change in magnetic field. As indicated by Figure 3.3 magnetostriction is nonlinear and furthermore the $d_{33,m}$ is quite low at or near zero magnetic field. To have an effective transducer it is desired to operate near a point where $d_{33,m}$ is at a maximum. In order to do this the MS material must be biased. Biasing is done by using a DC magnetic field (H_{DC}) to effectively move the ME laminate operating point to the maximum piezomagnetic coefficient value.

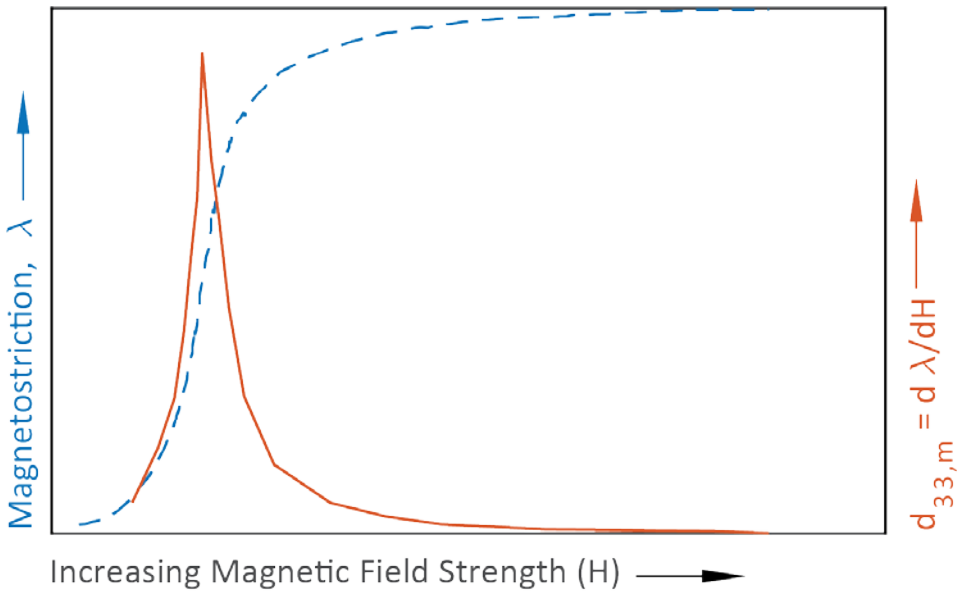

Figure 3.3: A typical magnetostriction profile and its derivative. Adapted from [29].

The general operational approach taken has been to use a DC magnetic field to find the desired operating point, or optimal bias, then use a superimposed AC magnetic

field of a much smaller amplitude to cause the structure to resonate[29]. To account for this biasing, which varies tremendously by material, Dong et al. added the variable β to equation 3.8. A value of $\beta = 1$ means the structure is optimally biased; a value of $\beta = 0$ means the structure is not biased at all[33]. Much like the quality factor, this component of the model has to be evaluated experimentally in that the optimal bias varies by geometry and material selection as well as with any preload induced into the structure. Work has been done to build self-biased ME structures that eliminate the need for biasing, however this research is still fairly premature and beyond the scope of this work[46].

Finally, the last consideration is anchoring. The model presented assumes an infinitely stiff anchor. Typically, vibrating transducer performance (such as for cantilever beams) is reduced when anchored to something compliant such as tissue, making this assumption questionable. However, an advantage to this design, is that due to the structure's vibrational symmetry, the equal and opposite motion of extension has a self-anchoring effect that minimizes loss through the anchor. Given this geometric advantage, this assumption was deemed suitable for this stage of research.

3.1.3 ME Laminate Model for Power Delivery Prediction

To derive the power output of the ME laminate utilizing the Dong et al. model a load simulating resistor was added to the equivalent circuit as shown in Magnetoelectric equivalent circuit with added load resistor, adapted from Dong et al. [30].

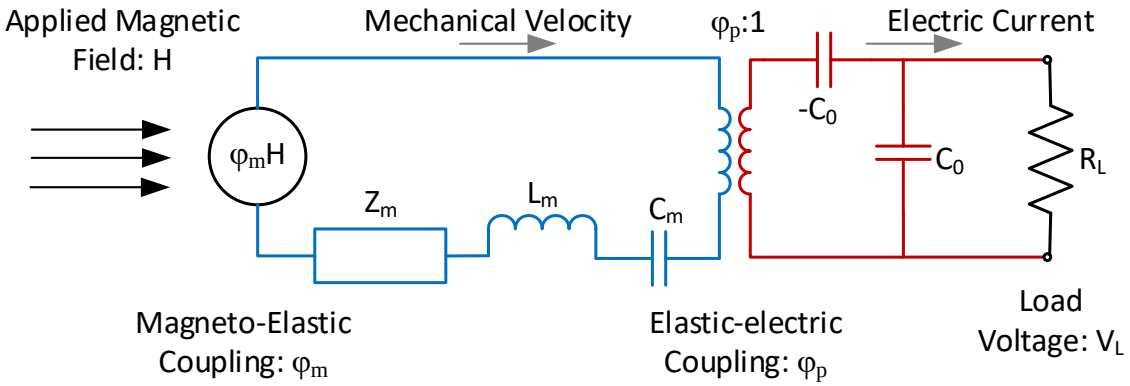

Figure 3.4: Magnetoelectric equivalent circuit with added load resistor. Adapted from [31].

With the new circuit model, using the same constitutive equations from before, α_{me} can again be derived using circuit analysis. To do this an equivalent impedance of the electrical portion of circuit is calculated as

$$Z' = \frac{R_L}{j\omega C_0 R_L + 1} - j\omega C_0 [\Omega] \tag{3.10}$$

where R_L is the resistance of the load resistor. Following the same process as demonstrated for the open circuit model the new equation for α_{me} becomes

$$\alpha_{me} = \frac{\partial V_{me}}{\partial H} = \left| \beta \frac{\varphi_p}{j\omega C_0 + \frac{1}{R_L}} \frac{\varphi_m}{Z_m + j\omega L_m + \frac{1}{j\omega C_m} + \varphi_p^2 Z'} \right| \left[\frac{V}{A/m}\right] \tag{3.11}$$

which by inspection can be seen to reduce down to equation 3.6 if R_L is set to zero. The peak load voltage (V_L) can then be calculated by

$$V_L = H_p|\alpha_{me}|\,[V] \tag{3.12}$$

where H_p is the magnitude of the sinusoidal magnetic field. Finally, the peak power (P_p) RMS power (P_{RMS}) are calculated respectively, as

$$P_p = \frac{V_L^2}{R_L}\,[W] \tag{3.13}$$

and

$$P_{AVG} = \frac{V_L^2}{2R_L}\,[W]. \tag{3.14}$$

3.1.4 Longitudinal-Transverse Model Augmentation

With a model for power output, the decision had to be made as to which laminate orientation should be utilized for this research The research done by Dong et al. ranks the orientations by ME voltage coefficient with L-L being the highest followed by L-T, T-L and, T-T [32], [33]. Consequently, the initial approach was to utilize the L-L method but was promptly inhibited by manufacturing constraint. As can be seen in Figure 2.2, PE transducers intrinsically require a conductive electrode on both of the pole faces (i.e. the faces perpendicular to the polling direction). In the case of L-L or T-L orientations the PE poling surfaces are very small and rapidly become unmanufacturable as the laminates are scaled down to the microscale. Alternatively, the relatively large pole faces of the L-T

and T-T laminates mitigate this problem and can allow for the circuit to even be passed through the conductive MS layer, simplifying attaching leads to the laminate. Based on the literature ranking, the obvious next best configuration for this study was L-T.

Based on this change, corrections in the previous model had to be made to reflect the new geometry layout as seen in Figure 3.5. The general equivalent circuit remained unchanged however, due to the change in orientation, equations involving the properties of the PM had to be updated. Particularly the piezoelectric voltage coefficient and elastic compliance became $g_{31,p}$ and s_{11}^{D} respectively now that the strain field was perpendicular to the poling direction. Also, the piezoelectric coupling factor was rederived as

$$\varphi_p = \frac{A_1 g_{31,p}}{t_p s_{33}^{D} \overline{\beta}_p} \left[\frac{N}{V}\right]. \tag{3.15}$$

A summary of the affected equations is shown in Table 3.2. By implementing these equations with others presented previously, the theoretical performance of the L-T configured laminate can be calculated.

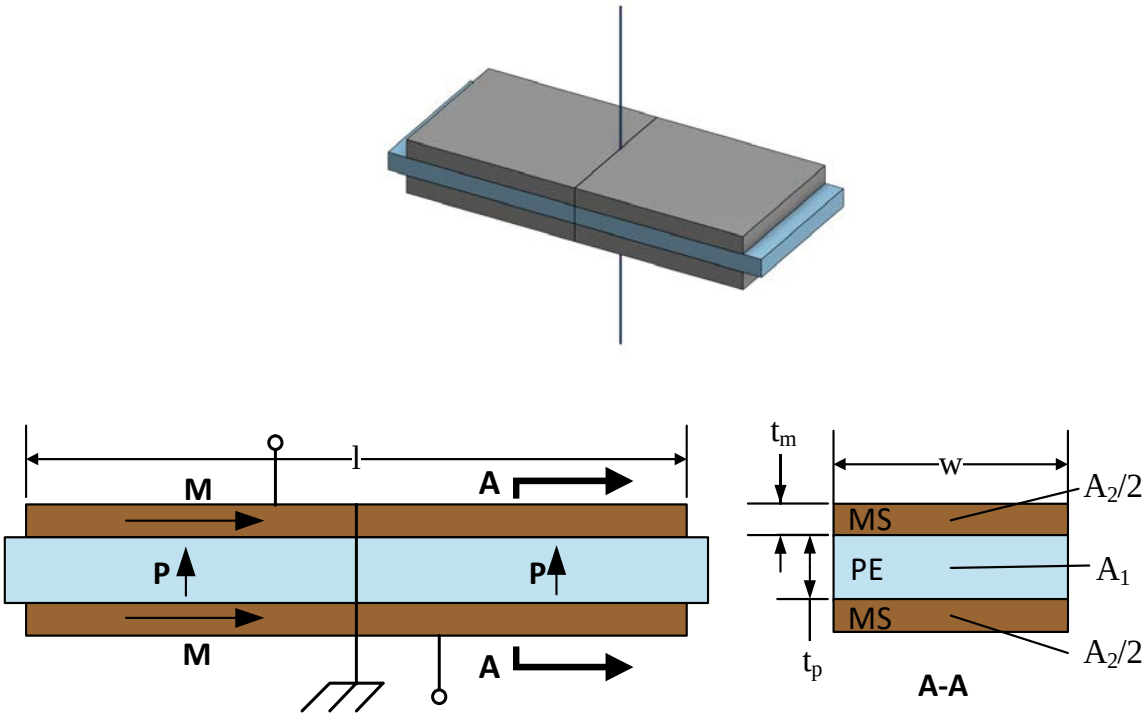

Figure 3.5: Geometry layout for L-T mode bimorph, arrows M and P show the magnetization and polarization orientation, adapted from [31].

Table 3.2: Corrected lumped parameters for L-T configuration [33].

Lumped Parameter Variable	**Constitutive Equation**
Effective Inverse PE Dielectric Constant, $\overline{\beta}_p$	$\overline{\beta}_p = \beta_p \left(1 + \frac{g_{33}^2}{s_{33}^D \beta_p}\right) \left[\frac{M}{F}\right]$
Piezoelectric Capacitance, C_0	$C_0 = \frac{wl}{t_p \overline{\beta}_p}\ [F]$
Magnetoelectric Wave Speed, v	$v = \sqrt{\frac{n}{s_{33}^H} + \frac{(1-n)}{s_{11}^D}}\ \left[\frac{m}{s}\right]$

3.2 Lumped Parameter Model for MME "Butterfly" Transducer

The second lumped element model to be discussed is that of the Mechano-Magnetoelectric (MME) transducer. Unlike the ME laminate model, there is not a well published lumped model for the specific geometry under consideration. Subsequently, the following lumped element model was obtained from a yet to be published parallel effort performed by Binh Duc Truong and Dr. Shad Roundy of the University of Utah's Integrated Self-powered Sensing Lab. The entire derivation can be found in [47].

3.2.1 MME Geometry and Model Summary

The new geometry proposed as shown in Figure 3.6, utilizes a single pizeoelectric bending laminate composed of a PE top sheet, a structural center sheet (S_{sub}), and another symetric PE bottom sheet to couple bending strain to an electric field. Strain is induced on the structure by anchoring the bending laminate in the center and adding opposite oriented permanent magnets at its ends. When a magnetic field is applied along the length of the structure the effect is a symetric cantilever or bending motion.

By making the structure a double cantilever beam, much like the ME bimorph, the stress transmitted through the anchor is ideally reduced to zero due to the counteracting motions of the two beams. This in turn means that anchor losses in mediums such as tissue should also be reduced.

The equivalent circuit model for the structure is shown in Figure 3.7. By inspection it can be seen that the model is fundamentally similar to the ME laminate model and shares the same parameters for the piezoelectric portion of the circuit.

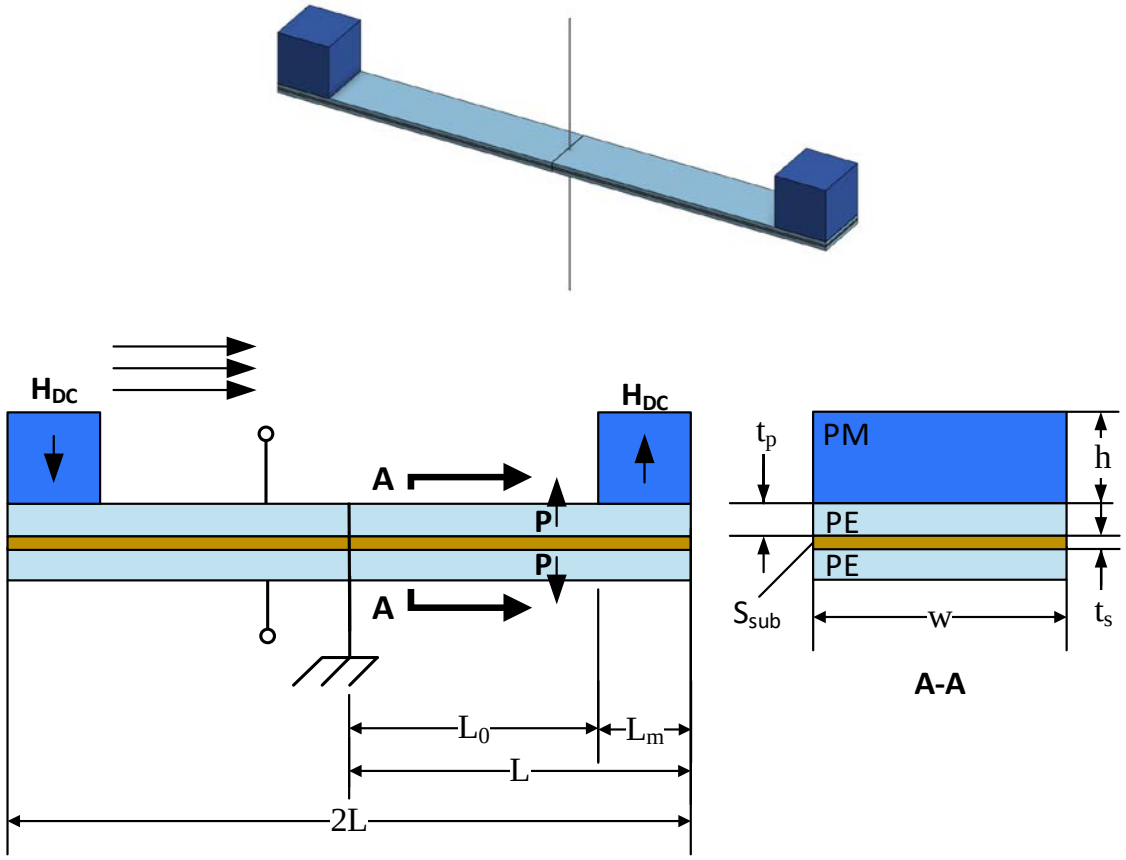

Figure 3.6: Geometry layout for the double cantilever MME structure. Arrows marked P indicate PE poling directions and arrows marked H_{dc} Indicate the orientation of the permanent magnetic fields.

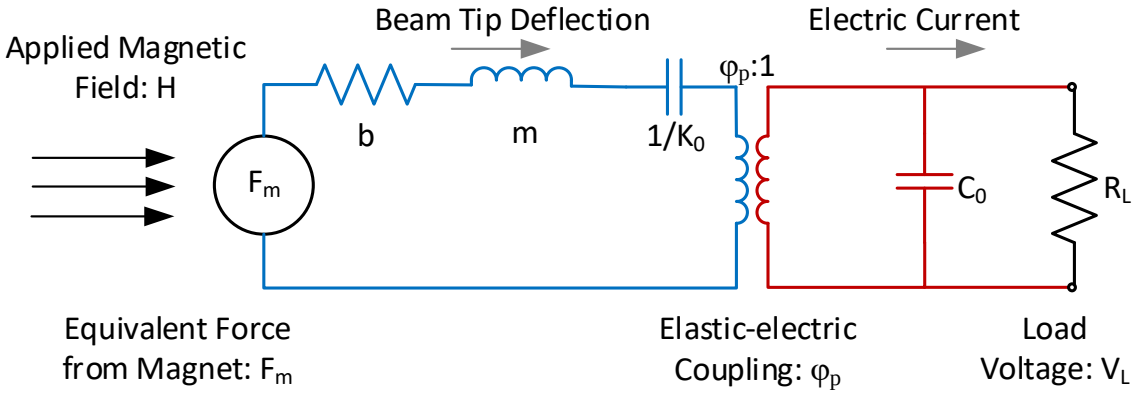

Figure 3.7: Lumped element equivalent circuit of double cantilever MME structure

The power output of the MME is calculated as

$$P = \frac{1}{2}\Delta K \frac{\omega^2 \tau}{1+\omega^2 \tau}|X_0|^2\ [W]. \tag{3.16}$$

where

$$\tau = R_L C_0\ [s], \tag{3.17}$$

$$\Delta K = \frac{\varphi_p^2}{C_0}\left[\frac{N}{m}\right], \tag{3.18}$$

$$\varphi_p = -\frac{4e_{31}w(2t_p + t_s)[3(M+m_b)L^2 - 3m_b L_0 L + m_b L_0^2]}{6(M+m_b)L^3 - 6m_b L_0 L^2 + 2L_0^2 L(M+2m_b) - L_0^3 m_b}\left[\frac{N}{V}\right], \tag{3.19}$$

and

$$|X_0|^2 = \frac{F_o^2}{\left[\omega b + \Delta K \frac{\omega\tau}{1+(\omega\tau)^2}\right]^2 + \left[K_1 - m\omega^2 - \Delta \mathrm{K}\frac{1}{1+(\omega\tau)^2}\right]^2}\ [m^2] \tag{3.20}$$

At optimal load resistance and natural frequency, the optimal average power is stated as

$$P_{AVG}^{opt} = \frac{F_0}{4b} M_1 \left(\sqrt{M_1^2 + 1} - M_1 \right) [W] \tag{3.21}$$

where

$$M_1 = \frac{\Delta \mathrm{K}}{b\omega_1} [W]. \tag{3.22}$$

In this case, the optimal load resistance is calculated as

$$R_L^{opt} = \frac{\sqrt{M_1^2+1}}{\omega_1 C_0} [\Omega]. \tag{3.23}$$

.

For the sake of simplicity, the variables and constitutive equations that compose equations 3.16-21 are summarized in Table 3.3. One can note that the model for the MME is a significantly more convenient than the Dong et al. derivation because there is a closed-form solution for the optimal load and power.

3.2.2 Limitations of the MME transducer model

With the new MME model presented, the limitations of the model haven't been fully explored experimentally, however by intuition some limitations can still be brought to light. Firstly, in Table 3.3 it is shown that the moment, M_b, due to the tip magnet, is converted into an equivalent point force F_m acting at an effective beam length l_{eff}. This assumption becomes increasingly more accurate as the magnet length L_m approaches zero. Conversely as L_m nears the entire beam length L the cantilever beam model would

be better described by a distributed load. The experiments done by Truong and Roundy, which were well correlated to their model, used a structure with an $L_m : L$ ratio of 1:4.8. It remains to be shown what the upper limit for the ratio of $L_m : L$ should be, but for the sake of this research it will be taken slightly conservatively as less than 1:4.

Another factor that the model overlooks is the strength of the beam itself, particularly the piezoelectric material. In fact, it is possible that the beam strength for the MME drives the $L_m : L$ ratio as much as the model's equivalent force assumption. In a linear model such as that presented by Truong and Roundy, an optimization of this model would likely lead to large magnets and large deflections, which may or may not be mechanically feasible. However, most piezoelectric materials are brittle and can fracture quiet easily so it is important to bound the structure design by ensuring that the bending strength of the PE material is not exceeded by the tip magnet. How this bounding can be done will be discussed in Chapter 5.

Table 3.3: Lumped parameters for MME transducer.

Lumped Parameter Variable	**Constitutive Equation**
Remnant Magnetic Polarization, J_r	Material Property
Magnet Density, ρ_M	Material Property
Substrate Density, ρ_s	Material Property
PE Modulus of Elasticity, E_P	Material Property
Substrate Modulus of Elasticity, E_s	Material Property
Damping Coefficient, b	Material Property
Effective PE stress constant, e_{33}	Material Property
Beam Length, L	Dimension
Beam Length to Magnet, L_0	Dimension
Magnet Length, L_m	Dimension
Effective beam length, l_{eff}	$l_{eff} = \frac{L + L_0}{2} [m]$
Beam Width, w	Dimension
Magnet Height, h	Dimension
Beam Substrate Thickness,t_s	Dimension
PE Layer Thickness, t_p	Dimension
Magnet Volume, V_m	$V_m = wL_m h_m \ [m^3]$
Substrate Volume, V_s	$V_s = wLt_s \ [m^3]$
PE Volume, V_{PE}	$V_{PE} = 2wLt_p \ [m^3]$
Magnet Mass, M	$M = \rho_M V_m \ [kg]$
Beam Mass, m	$M = \rho_s V_s + \rho_{PE} V_{PE} \ [kg]$

Table 3.3: Continued

Beam Mass, m_b	$m_b = \rho_s V_s + \rho_{PE} V_{PE}\ [kg]$
Equivalent Mass, m	$m = M + \frac{33}{140} m_b$ [m]
Magnet Moment, M_b	$M_b = J_r V_m H_{AC}$ [Nm]
Equivalent Moment Force, F_m	$F_M = \frac{3M_b}{2l_{eff}} [N]$
Short-circuit Stiffness, K_0	$K_0 = \frac{3(YI)_c}{l_{eff}^3} \left[\frac{N}{m}\right]$
Optimal Load Stiffness	$K_1 = K_0 + \Delta K \left[\frac{N}{m}\right]$
Composite Flexural Rigidity, $(EI)_c$	$(EI)_c = 2E_p \left[\frac{2wt_p^3}{12} + 2wt_p \left(\frac{t_s + 2_{tp}}{2}\right)^2\right] + E_s \frac{wt_s^3}{12}\ [Nm^2]$
Piezoelectric Capacitance, C_0	$C_0 = \frac{wl}{2t_p \beta_p}\ [F]$
Loaded Natural Frequency, ω_1	$\omega_1 = \sqrt{\frac{K_1}{m}} \left[\frac{rad}{s}\right]$

CHAPTER 4

EXPERIMENTAL VALIDATION OF TRANSDUCER MODELS

To ensure that the models being implemented into the numerical optimization study yielded credible results, particularly with regard to the power output, it was necessary to verify them experimentally. The chosen approach was to build millimeter (as opposed to micrometer) scale transducers, characterize them, and then compare their characterization data with the model predictions. Millimeter scale transducers were used to avoid prematurely expending time and resources on a microfabricated design before completion of the optimization.

4.1 Experimental Setup

In order to characterize any ME transducer a well understood magnetic field must be generated to serve as a baseline transmitter. In this case it was decided to build a single axis nested Helmholtz Coil, given their exceptional magnetic field uniformity. Leveraging work done by Abbott on nesting tri-axial coils, the field generator was designed with an exterior DC coil pair and a nested AC coil pair built in such a way to allow for uniform superimposition of fields[48]. By superimposing the two fields, ME transducers could be both biased with the DC field and driven with the AC field. The diagram for this setup is shown in Figure 4.1

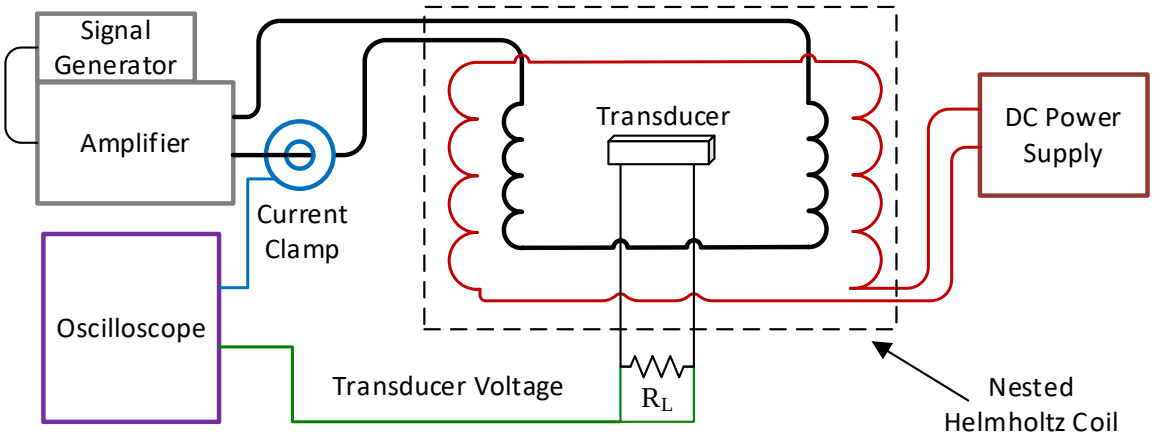

Figure 4.1: Magnetoelectric transducer experimental test setup diagram.

4.1.1 Nested Helmholtz Coil Design

The performance goal of the setup was to deliver an AC magnetic field (H_p) of 2-Oe (2 G in air) at 150 kHz with a 40-Watt 50Ω amplifier with no additional circuitry (IE tuned resonating capacitors) and a DC magnetic field (H_{DC}) of 16-Oe without exceeding the safe wire gauge current. Subsequently, the geometry of the coils was bounded by the minimum active area needed to fit transducers and the maximum coil size that could be driven with accessible amplifiers. Using the equations from Abbott's paper to approximate magnetic field levels, the geometry in Table 4.1 was produced[48].

Table 4.1: Nested Helmholtz Coil geometry.

Specification	**AC Coil**	**DC Coil**
Coil diameter (center of cross-section)	91	133 mm
Nominal coil cross-section	4.9 mm x 4.9 mm	4.9 mm x 4.9 mm
Optimal coil separation spacing	46 mm	67 mm
Wire gauge	16	20
Number of turns	9	25

4.1.2Nested Helmholtz Coil Performance

The geometry resulted in the built device shown in Figure 2.1. Built with 3D printed ABS and hand coiled copper magnet wire, the produced field was found to be very uniform. Using an AlphaLab UHS2 gauss meter, the AC coil was measured to have only 2% field variation over ±1.5 cm at the coil origin (the point colinear to the coil axis and equidistant from the inner coil faces) along the axial center line. The DC coil had less than 5% variation over the same length. For this and all other work the AC coil was driven by a Tektronix AFG1022 signal generator and either a E&I 210 or a Rigol PA1011 amplifier. The DC coils were driven with a B&K Precision 9201 power supply.

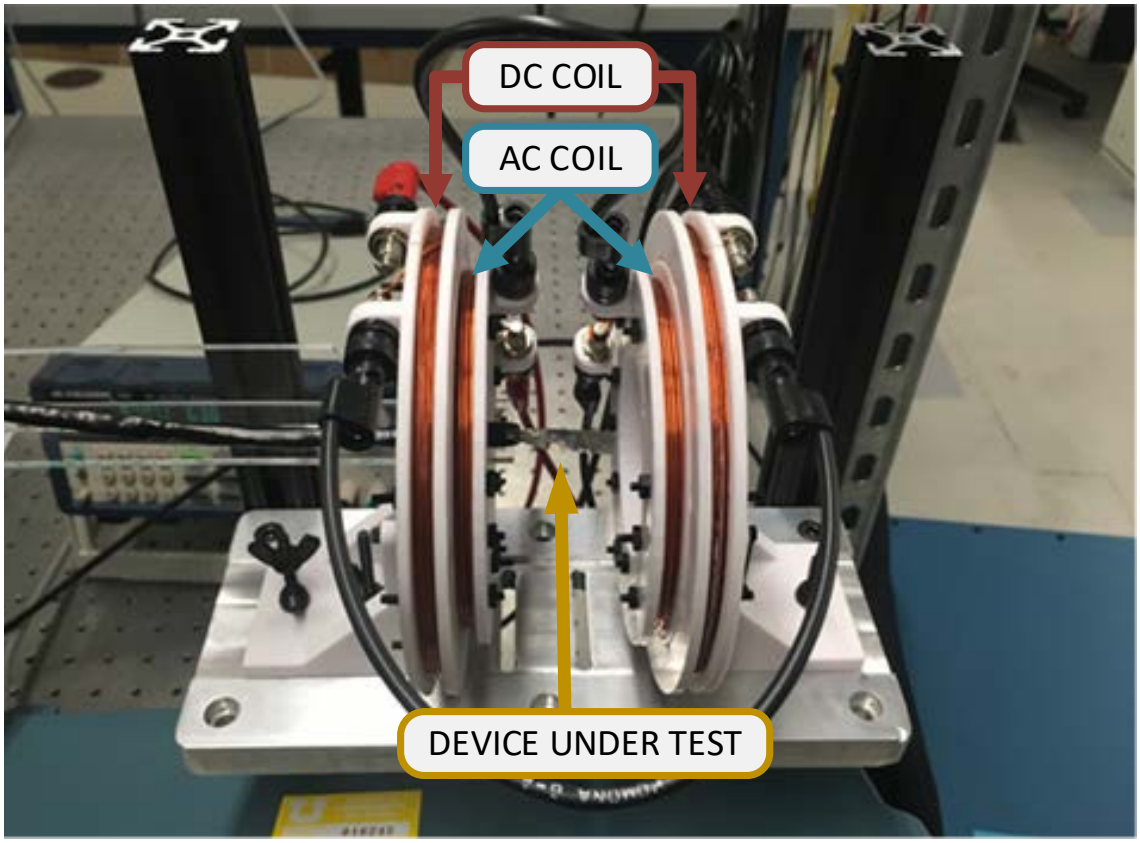

Figure 4.2: Nested Helmholtz Coil built for experimental validation.

Given the difficulty of measuring AC magnetic fields during experiments with ME and MME transducers, the linear relationship of electric current to field strength was used to create a calibration curve. This was done for the AC coils by measuring field magnitude at the coil origin while a 10kHz driving current was increased, ensuring that the DC coils were shorted out. To characterize the DC coils, the process was reversed, driving them under an AC load to utilize the same AC sensor, ensuring that the AC coils were now shorted. By so doing the coil field strength could be monitored from the output of a current clamp rather than a bulky, narrow frequency AC magnetic field sensor during any subsequent ME transducer testing. Also, to get a better understanding of the coils, their inductance was measured using a circuit analyzer. The results of this coil characterization are shown in Table 4.2.

Table 4.2: Built nested Helmholtz Coil performance and predictions.

	AC Coil	**DC Coil**
Optimal Spacing	52 mm	Driven by AC Coil
Total inductance predicated	7.3 µH	88 µH
Total inductance measured (alternate coil open circuit)	38 µH	410µH
Total inductance measured (alternate coil short circuit)	30 µH	Not Measured
Coil calibration (alternate coil short circuit)	.502 Oe/A (R^2=.9998)	1.350 Oe/A (R^2=.9999)
Predicted field levels	2 Oe Peak at 150Khz & 40W	16 Oe at 6A DC
Realized field levels	.5 Oe Peak at 150kHz & 40W	8.1 Oe at 6A DC

From examination of the table it is seen that both the field performance and predicted inductance were far below the design predictions made. In reviewing the equations used, the discrepancy was explained as it became evident that the approximations from Abbott were better suited for coils with much smaller diameter wire and a great number of turns[48]. Additionally, the work done here also failed to account for the reduction in performance caused by the coupled inducive effect of nesting two sets of coils on the same axis. All told, enough margin was given for the desired field levels that the design was still useful for this research. Nonetheless, a better method for design of coils for ME transducers should be implemented, or at the very least, a design should be verified before manufacture with another tool such as FEA.

4.1.3 Additional DC Field Biasing Measures

During this work it became evident that it would be difficult to build DC coils large enough to bias structures made of Galfenol or Terfenol-D. As built the DC coils were capable of biasing Metglas structures which requires a bias on the order of 1-10 Oe [29]. To bias Galfenol or Terfenol-D, which require bias fields 100s of Oe, many different approaches can be taken[30]. Two parallel N52 Neodymium magnets were used as shown in Figure 4.3. By adjusting the distance between the two magnets with a 3d printed stage as shown in Figure 4.5 the field seen by the centered transducer can be adjusted such that $\beta = 1$.

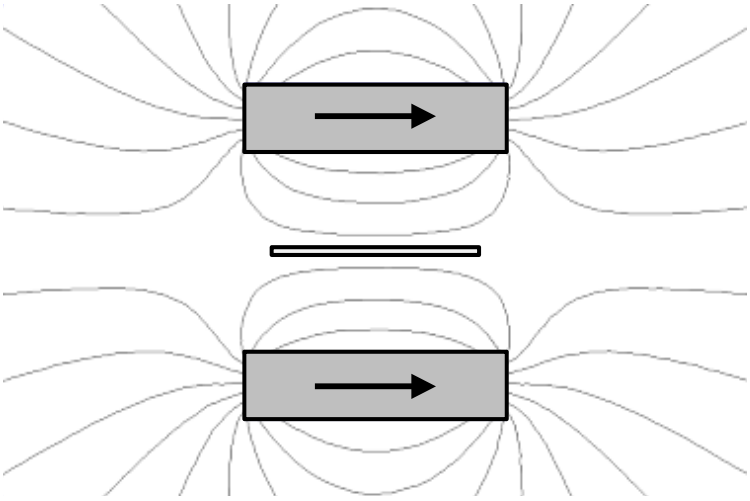

Figure 4.3: Biasing magnet arrangement and resulting field lines. Transducer is shown in between the two magnets.

4.2 Fabrication of ME Transducers

Two ME transducers were built to validate the model. Two material structure combinations were built, a Galfenol and lead zirconate titanate (PZT) laminate as well as a Metglas 2605SA1 and polyvinylidene fluoride (PVDF) laminate. Terfenol-D was avoided due to the difficulties associated with machining a brittle, pyrophoric material.

4.2.1 Galfenol-PZT Transducer

To build the Galfenol-PZT device, 25.4mm diameter, TdVib Galfenol was cut using electrical discharge machining into two 10mm x 20mmx x 370µm sheets poled along the 20mm length. The PE material used was 1.02mm thick Piezo Systems PZT-5A (T140-A4E-602) which was cut using a diamond blade dicing saw to a single 10x20mm sheet polled through the thickness. The three layers were then bonded together such that the PE layer was sandwiched between the ME layers. EPO-TEK H20S silver filled (conductive) epoxy was used to glue the laminate.

The epoxy was cured using a heat press, following the epoxy's minimum cure instructions. Finally, two .635 mm right angle header pins were bonded to the top and bottom Galfenol. This bond was done using MG Chemicals silver conductive epoxy given that the joint wasn't structural. This epoxy was cured overnight at room temperature. The resulting transducer can be seen in Figure 4.4

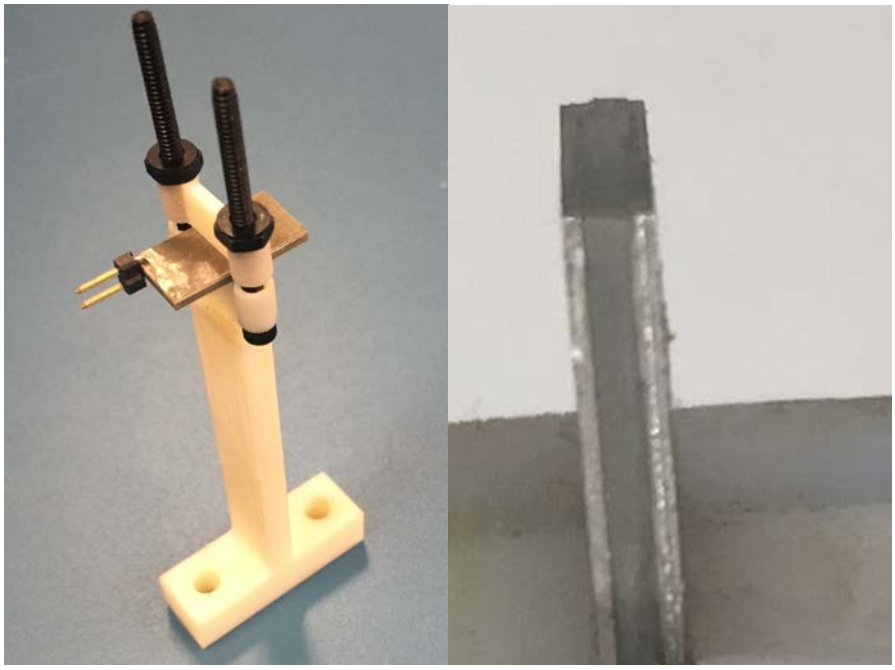

Figure 4.4: Galfenol-PZT ME transducer, shown anchored at its center (left), and zoomed in on the cross section (right).

4.2.2 Metglas-PVDF transducer

The Metglas-PVDF device was built in a fashion similar to that of the Galfenol-PZT. Raw 23μm thick 2605SA1 Metglas was cut using scissors into two 10x20mm layers. The nature of amorphous Metglas is such that magnetostriction occurs at any orientation in the sheet plane so poling direction was unimportant. To match the very thin Metglas, metalized PVDF (TE 1-1004347-0) was used. These sheets themselves were a

sandwich of 28μm PVDF with 6μm silver ink electrodes on the top and the bottom, poled through the thickness.

These sheets were also cut to 10x20mm; however, a small tab was left so that electrical leads could be attached to the PE while using a non-conductive epoxy. In particular the nonconductive epoxy EPO-TEK H70E was used for its slightly thinner minimum bond line of less than 20 μm compared to the silver filled alternative which was measured on the Galfenol-PZT device to be about 35 μm. As before, the epoxy was cured in a heat press at the minimum prescribed cure. Similar leads were also bonded as before, however this time on the center flange of the PVDF. The final structure can be seen in Figure 4.5.

Figure 4.5: Metglas-PVDF ME transducer with bonded leads visible.

4.3 Galfenol-PZT Device Characterization and Model Comparison

The structures were characterized, beginning with the Galfenol-PZT device. The process to do so began with first optimizing the magnetic bias field. Next open circuit frequency sweeps were done to determine the structure's natural frequency and the system's repeatability. Finally, loaded circuit frequency sweeps and load optimization were done.

4.3.1 Optimal Bias Field

To determine the optimal field bias for the transducer it was mounted between two adjustable magnets as shown in Figure 4.6. While operating the coils at 70 kHz (near resonance), the open circuit output voltage of the transducer was measured as the distance between the transducer and the magnets was varied. The distance between the magnet's inner faces, for which voltage was maximized, was found to be 1.70 inches. The transducer was located in the center as is shown. Moving the magnets closer or further apart diminished voltages as the structure became over or under biased respectively.

The DC bias field component parallel to the transducer length was measured along the length of the transducer with an Alphalab GM1-ST DC gauss meter yielding an average strength of 156 Oe with ±20 Oe deviation from average across the length of the device. Literature for bias field levels of Galfenol transducers is sparse, however for stiffer Terfenol-D transducers have reported bias fields of 200-500 Oe, depending on the

structure design so the value of 156 Oe seems reasonable[31], [42]. From this point forward, all Galfenol experiments were done under the DC bias field of 156 Oe, making the assumption that this was where $\beta = 1$ for the built transducer.

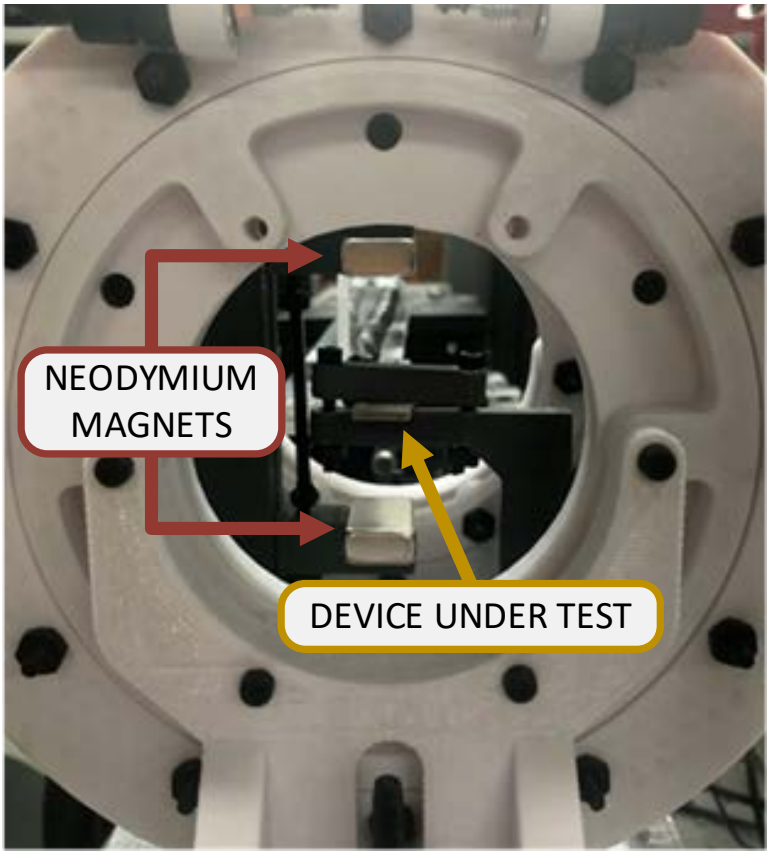

Figure 4.6: Galfenol-PZT structure mounted in bias field stage. The stage is located central to the visible Helmholtz Coils.

4.3.2 Open Circuit Voltage Testing

Having found where $\beta = 1$, the transducers open circuit performance was tested. Using a sinusoidal wave form, the coils were swept from 50 to 150 kHz at a rate of 12.5 kHz/s (10 second total duration). The coil amplitude was set at $H_p = .1$ Oe @50kHz,

however this value attenuated as the sweep progressed due to the increasing coil impedance. To compensate for this the magnetic field level and open circuit transducer voltage were measured simultaneously and then normalized for all of the sweeps done.

The normalization was done by performing an FFT on the signals then dividing the resulting transducer voltage amplitude by the field amplitude. The result, known as a linear transfer function, was then multiplied by $H_{RMS} = .707$ Oe to find the open circuit RMS voltage, V_{ORMS}, across the sweep frequency. It should be noted that this normalization does make the assumption that the transducer performance is linear, as does the model to which it will be compared. This assumption is common for many transducers and was validated experimentally for the ME transducer design by Bian et al [49].

For these first open circuit tests, to ensure that the results were repeatable, the transducer was swept nine times. Additionally, after each sweep the stage holding the transducer was removed then replaced; after every 3rd sweep the transducer was also removed from the bias structure entirely then re-clamped. The results of these sweeps can be seen in Figure 4.6

By examining the plots, it is evident that the system is quite consistent in that at natural frequency the standard deviation is only about 4.5% of the average value. The average natural frequency (ω_s) of the system was found to be 71.3 kHz with an average quality factor Q_m of 62.65.

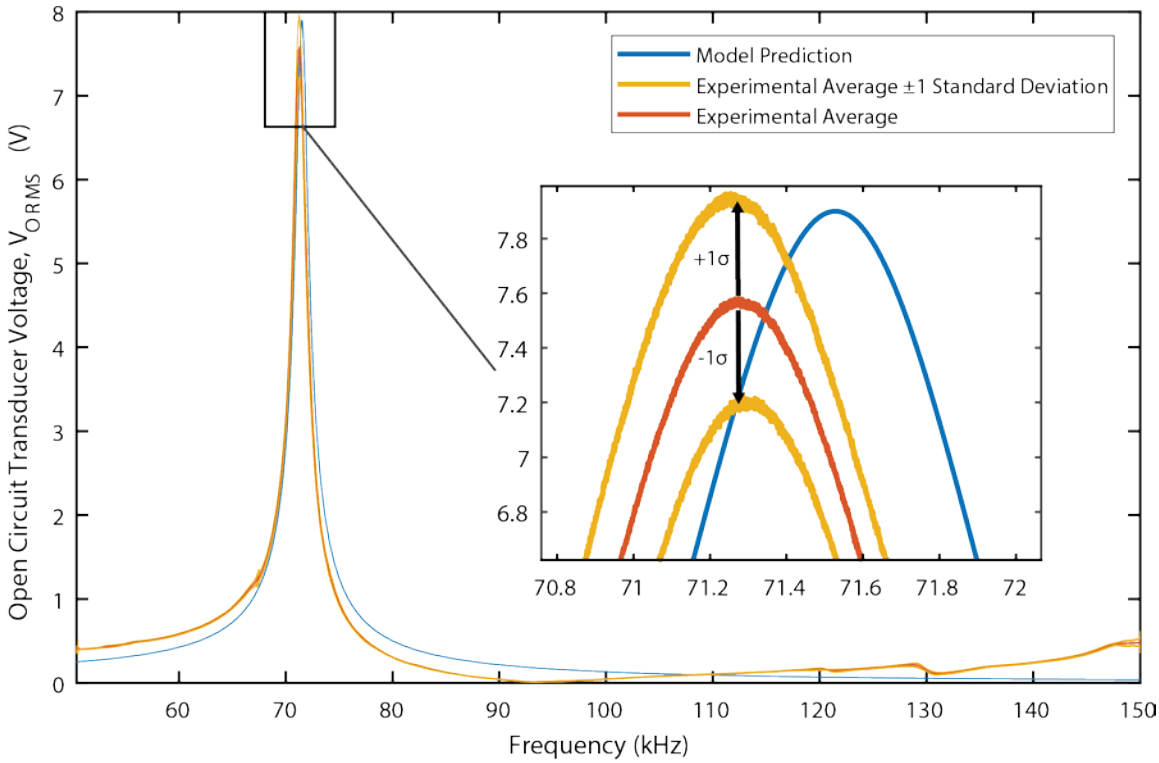

Figure 4.7: Repeated open circuit voltage vs frequency. Experimental Average, upper and lower deviation and model prediction shown.

4.3.3 Tuned Comparison Model

Also shown in Figure 4.6 is a curve for what the Dong et al. model predicted for the structure performance. The model was fed the geometric parameters of the tested structure and the material properties shown in Table 4.3. By matching the model's quality factor to that of the experiment and choosing $d_{33,m} = 15\ nm/A$, it is evident that the open circuit model matches the experimental result quite well.

Table 4.3: Material properties used for Galfenol-PZT laminate model[50],[51].

Property	Value
Piezo Systems PZT-5A4E	
Piezoelectric voltage coefficient, $g_{31,p}$	-11.6 x 10^{-3} Vm/N
Density, ρ_{pe}	7800 kg/m^3
Piezoelectric compliance, $s_{11,p}$	15 x 10^{-12} m^2/N
Relative Dielectric constant, K_3^T or $(1/(\beta_p \epsilon_0)$	1800
TdVib Galfenol	
Piezomagnetic coefficient, $d_{33,m}$	15-30 nm/A (15 used)
Density, ρ_{ms}	7800 kg/m
Magnetostrictive compliance, s_{33}^H	12.5-25.0 x 10^{-12} m^2/N (16.7 used)

The choice of 15 nm/A was justified by the manufacturer's reporting that $d_{33,m}$ decreases as the Galfenol becomes preloaded. In the case of the ME laminate, the stiffness of the piezoelectric material, resisting the motion of the Galfenol, acts as such a preload. The problem is further exacerbated as the volumetric layer ratio, n, becomes lower than optimal, or in other words there is too much PE material given the amount of MS material. This was the case for the Galfenol-PZT transducer which, through an error in arithmetic, ended up built with a n of 0.42 as opposed to an optimal 0.79 given the materials used. Correspondingly it can be assumed value of $d_{33,m}$ would be higher if n were optimal.

4.3.4 Optimal Load and Power Delivery

To determine the optimal load resistance, the coil was driven at 71 kHz while the load resistance swept from .1 to 5 kΩ using a substitution box. The power delivered was

then calculated using the measured voltage across the load resistance. The results of this procedure are seen in Figure 4.8.

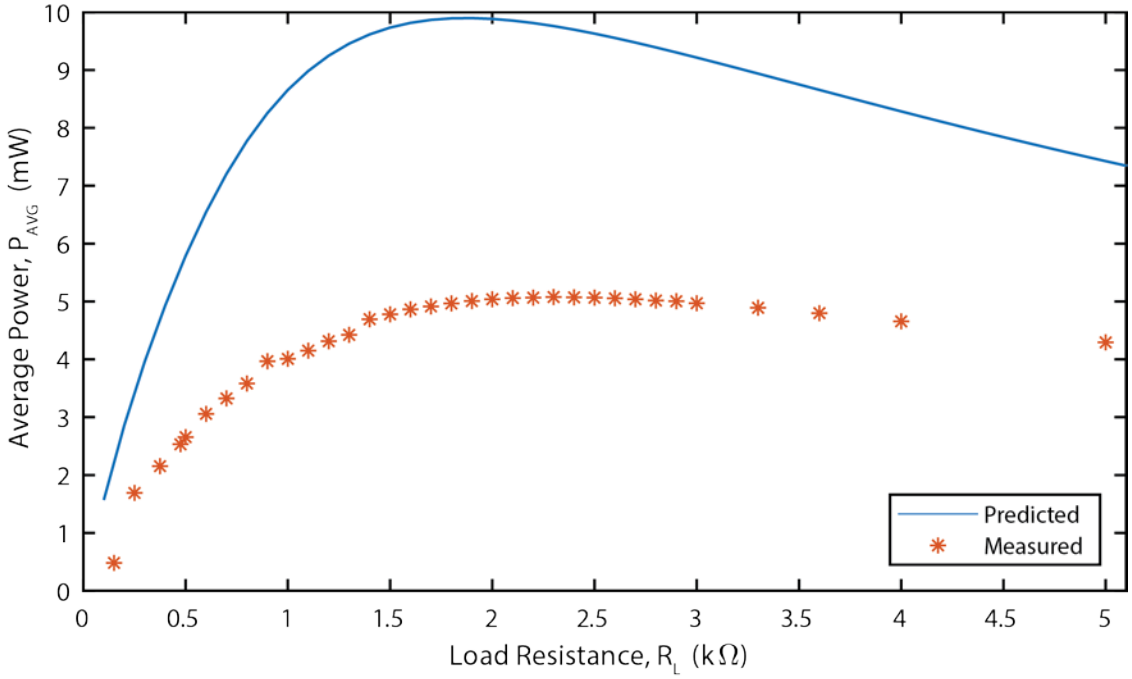

Figure 4.8: Power output vs load resistance for Galfenol-PZT device operating at 71 kHz.

In particular, the transducer was found to have a max P_{AVG} of 5.01 mW at R_L = 2.3kΩ as compared to the model which predicted the max P_{AVG} to be 9.95 mW at R_L = 1.9kΩ. These results were promising in that the load resistance and curve shape of the experiment were sufficiently similar to that of the model. For the Galfenol-PZT transducer the model also overpredicted power delivery by almost double what was found experimentally.

To examine this discrepancy another frequency sweep was performed. For this sweep the circuit was loaded optimally at R_L = 2.3kΩ. Under open circuit conditions the model and experiment had matching mechanical quality factors (Q_m) because of the tuning done. In the loaded case, the mechanical quality factor can no longer be measured

because of the attenuation caused by the load resistor. In lieu of Q_m a loaded circuit quality factor (Q_p) is measured. The results, as seen in Figure 4.9, indicate that despite the matching mechanical quality factors at open circuit, the power experiments showed a loaded circuit output quality factor that was about 20% less than that predicted by the model.

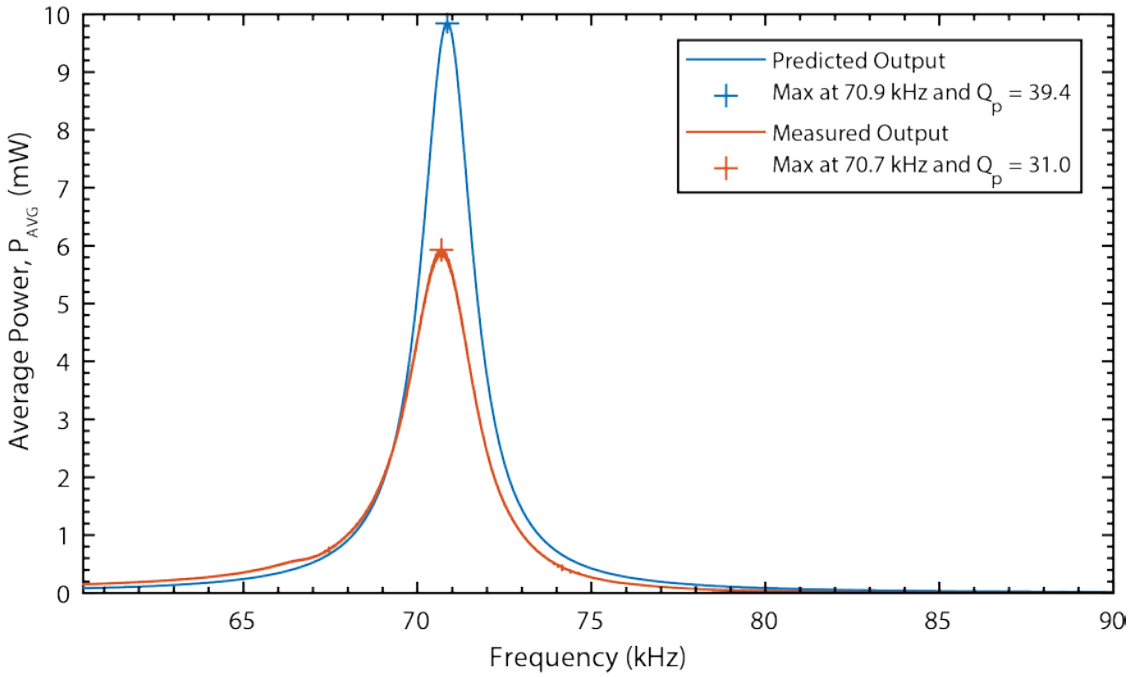

Figure 4.9 Power output vs frequency for the Galfenol-PZT device loaded at 2.3kΩ.

To explain the difference in quality factors, the initial reaction was to look to the model for neglect of some sort of damping, however errors in the model appeared unlikely based on the results witnessed with the Metglas-PVDF structure as will be discussed in Section 4.3. A better explanation would be uncertainty in the parameters being fed into the model, particularly those relating to the Galfenol. As was discussed in section 3.1.2, the magnetostriction constant, d_{33h} is a largely nonlinear property which

varies based on field bias, H_{DC}, as well as the laminate's preload. Additionally, if the magnet bias deviates from optimal the β factor will decrease, lowering power output. On the experimental side of things low permittivity of Galfenol led to the use of permanent magnets as opposed to a much more uniform Helmholtz coil for the experiments. Based on these realities, it is possible that the optimal transducer bias shifted as the transducer was loaded with a resistance, or the coarse adjustments of the bias field tuning caused β to not actually be equal to 1. Chapter 6 covers potential ways to reconcile this difference.

4.4 Metglas-PVDF Device Characterization and Model Comparison

The characterization of the Metglas-PVDF Device followed the same process as was used for the Galfenol-PZT device. Additionally, with the exception of the bias field magnets, the same equipment and signal processing was used to perform the experiments as was described in section 4.3. The device was mounted as shown in Figure 4.10 and with the AC coils operating at 96 kHz, the DC coils were used to find the optimal open circuit H_{DC} of 22 Oe which is on the same order of magnitude as other reported Metglas transducers [29].

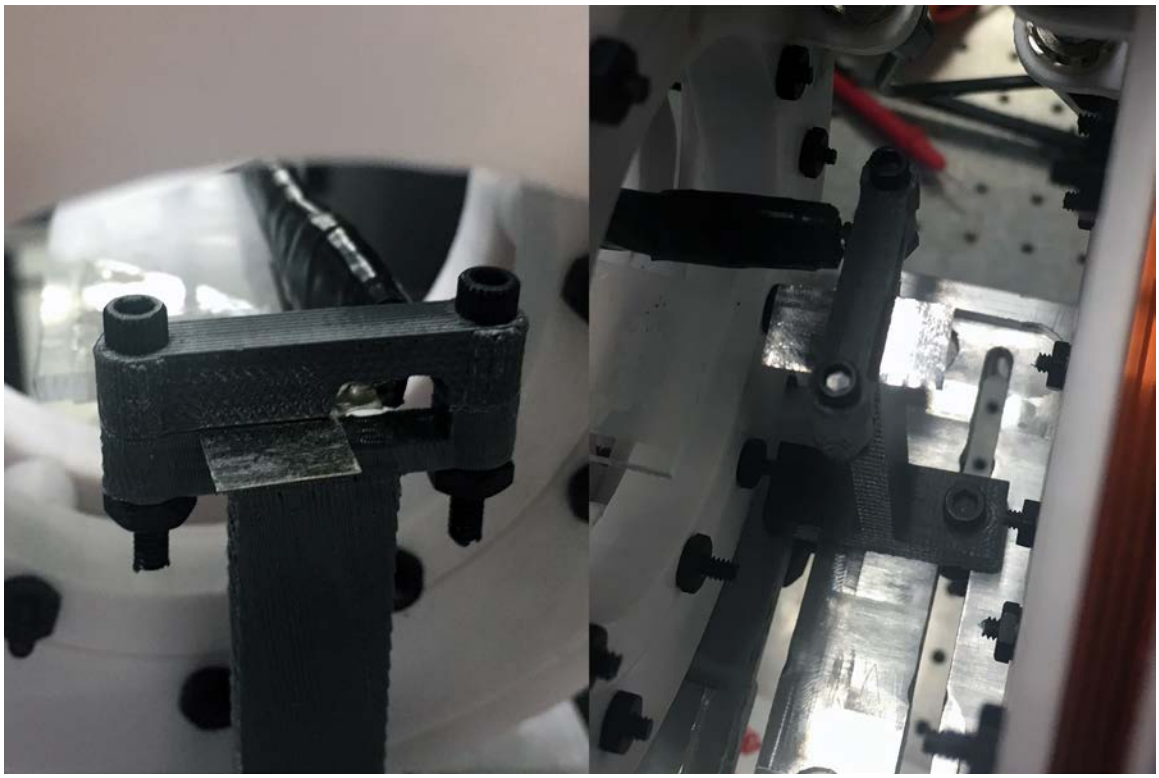

Figure 4.10: Metglas-PVDF Transducer as mounted, shown from the side and top.

4.4.1 Open Circuit Voltage Testing and Tuned Model

With the bias field tuned, open circuit frequency tests were conducted which resulted in consistent results such as those shown in Figure 4.11. The laminate exhibited a Q_m of 34.0, which was then used to adjust the model prediction which is also shown. In addition to the quality factor, the material properties shown in Table 4.4 were also used to generate the model prediction.

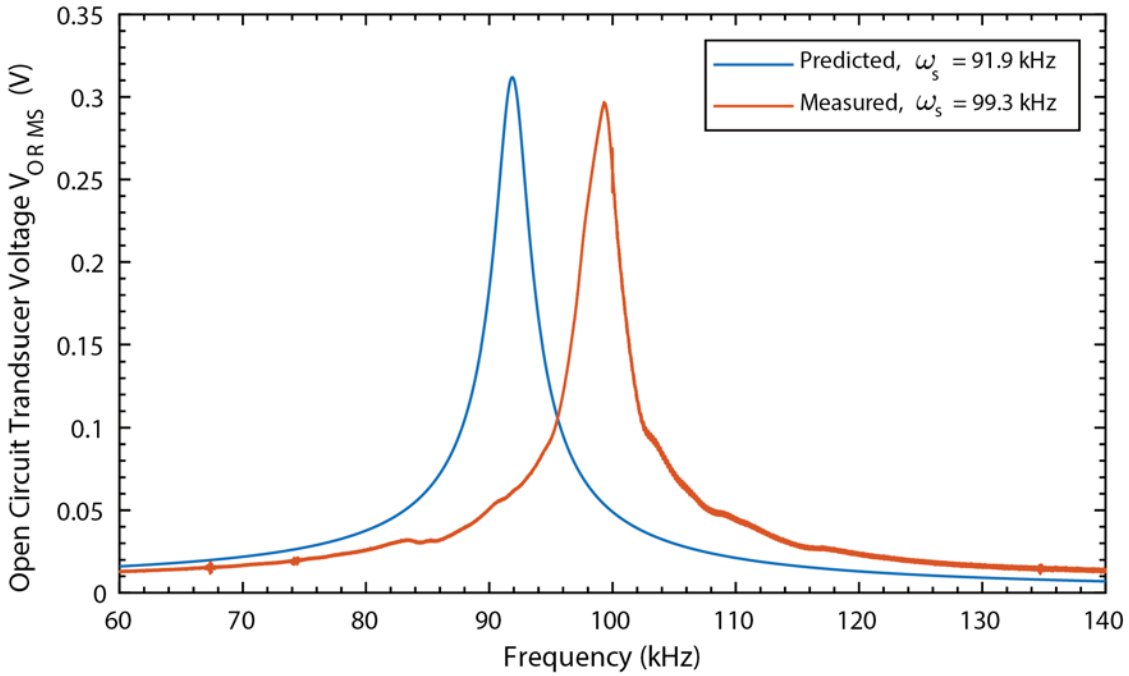

Figure 4.11: Metglas-PVDF open circuit voltage versus frequency.

Table 4.4: Material properties used for Metglas-PVDF model[28], [29], [52], [53].

Property	Value
TE Metalized PVDF	
Piezoelectric voltage coefficient, $g_{31,p}$	216 x 10^{-3} Vm/N
Density, ρ_{pe}	1780 kg/m^3
Piezoelectric compliance, $s_{11,p}$	3.7 x 10^{-10} m^2/N
Relative Dielectric constant, K_3^T or $(1/(\beta_p \epsilon_0)$	12
Metglas 2605SA1	
Piezomagnetic coefficient, $d_{33,m}$	25-50 nm/A (25 used)
Density, ρ_{ms}	7180 kg/m
Magnetostrictive compliance, s_{33}^H	9.09 x 10^{-12} m^2/N

Further examination of the figure, shows that the built transducer appears to follow the model closely with the exception of the increased natural frequency and

slightly attenuated performance. This was expected since the Dong et al. model does not account for the relatively large epoxy thickness (approximately 20-35% of the total laminate thickness) or the silver electrodes which together should stiffen the structure and reduce performance due to interface losses through the adhesive.

4.4.2 Optimal Load and Power Delivery

The trends seen in open circuit testing were also manifest as the load resistor was optimized and in the subsequent power output characterization. As before, the load resistance was swept and plotted to determine the built transducers optimal resistance. Given that the optimal frequencies did not match one another, the prediction and the built device were swept at their respective natural frequencies. As is shown in Figure 4.12 the optimal load was found be about 1.9 kΩ as compared to the prediction of 2.3 kΩ.

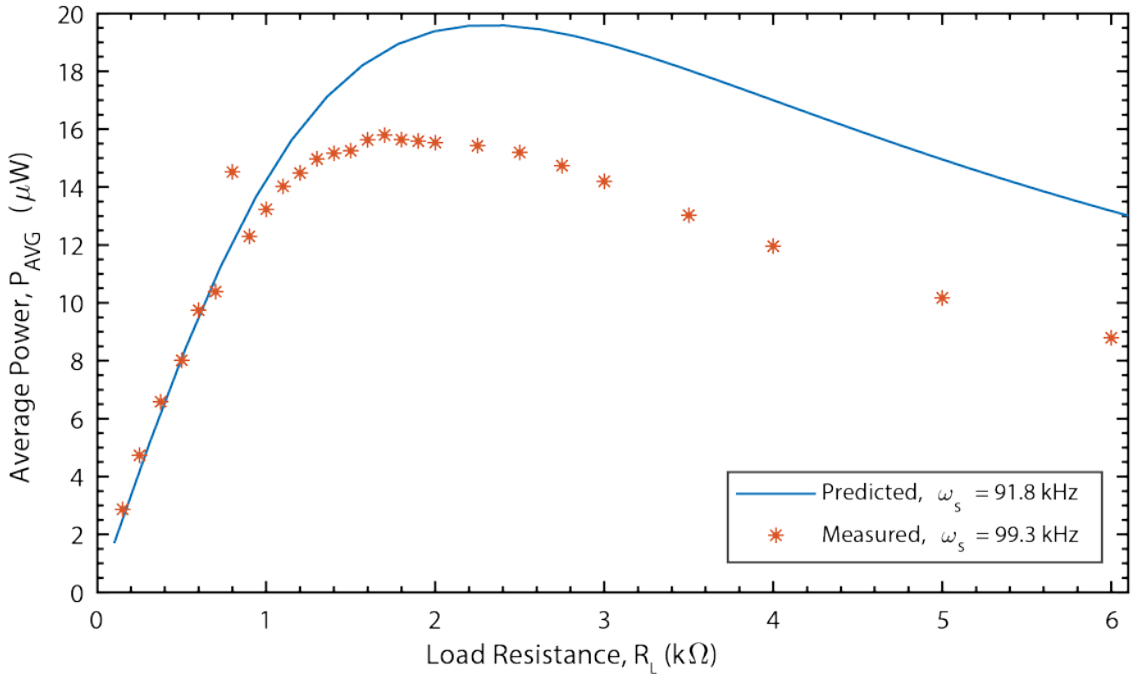

Figure 4.12: Power output vs load resistance for Metglas-PVDF device operating at natural frequency

Using the optimal load resistance of 1.9 kΩ, the power output was measured as frequency was swept and compared to the tuned model performance. Much like the open circuit resistance, the transducer appeared to have slightly attenuated performance from the prediction (see Figure 4.13) but adequate power delivery given the components of the transducer which were not taken into account.

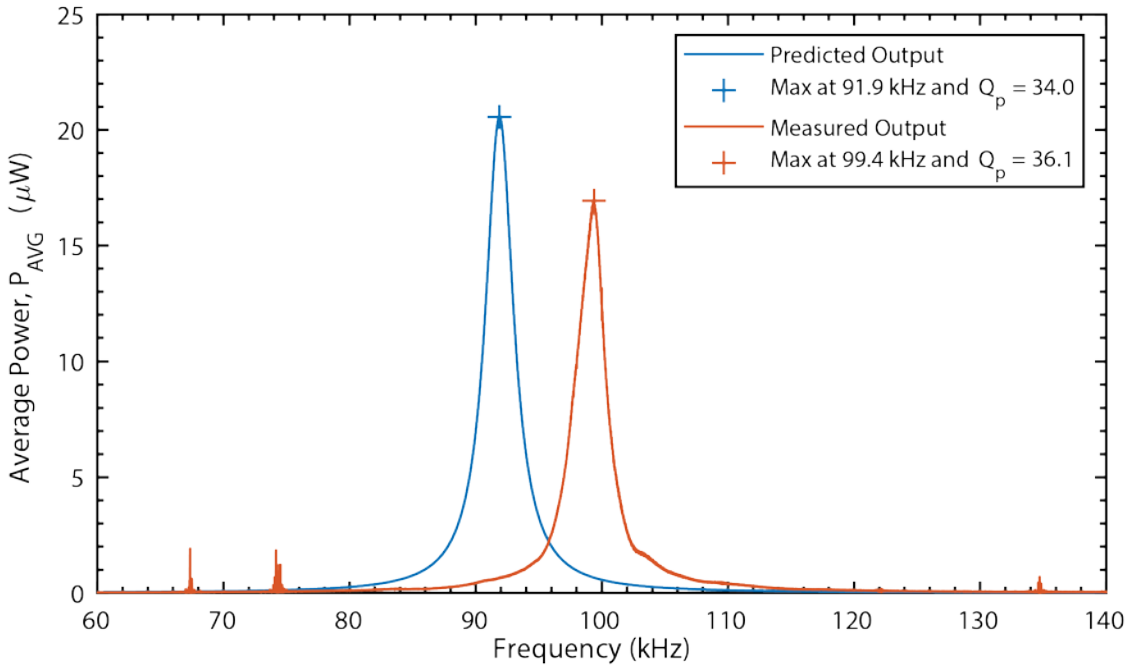

Figure 4.13: Power output vs frequency for the Metglas-PVDF device loaded at 1.9kΩ

When compared to the Galfenol-PZT transducer, the Metglas-PVDF transducer clearly showed better correlation to its model predictions. By looking at the model validation globally it is evident that the model is reliable to the extent that the parameters it is fed with are accurate. If a greater degree of accuracy were desired for these particular

transducer designs, a more rigorous study involving multiple structures of the same design would be suggested as well as FEM correlation. However, given the use of this model as an explicit equation for optimization and comparison and not for absolute performance values, the results of this validation were sufficient for use in the design optimization.

4.5 MME Model Validation

As was indicated previously, a parallel effort went into the derivation of the MME model. As such, work comparable to the ME validation and involving the same test equipment was also done to experimentally validate the transducer model. Both the model development and validation were done by Binh Duc Truong and Dr. Shad Roundy. Shown in Figures 4.14 and 4.15 are the experimental results of a built transducer compared to the developed model. The transducer used for validation was a 32.55 mm long, 3.175 mm wide and .38 mm thick bimorph made of PZT-5A with a .14 mm brass center substrate. The magnets used were Neodymium cubes with a 3.175 mm edge length.

Figure 4.14 shows the experimental and predicted power delivery over a frequency sweep. Here it is visible that, at the given field level, the maximum power outputs and operating frequencies of the model and built device match up such that their differences are almost indistinguishable. Only by increasing the magnetic field levels, as shown in Figure 4.15, does the model begin to slightly deviate from the experimental results. Truong and Roundy attribute this to the fact that the built device is not perfectly symmetrical. These results indicate that the model derived is more than adequate to be

used in a parameter optimization. The entirety of Truong and Roundy's model derivation can be seen in [47].

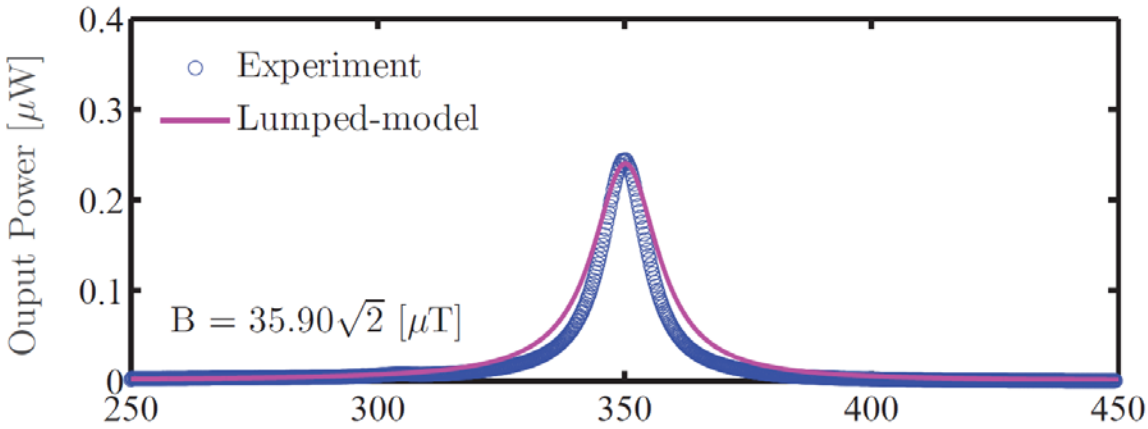

Figure 4.14: Experimental and modeled MME transducer power output across frequency. Figure reproduced with permission from Binh Duc Truong and Dr. Shad Roundy [47].

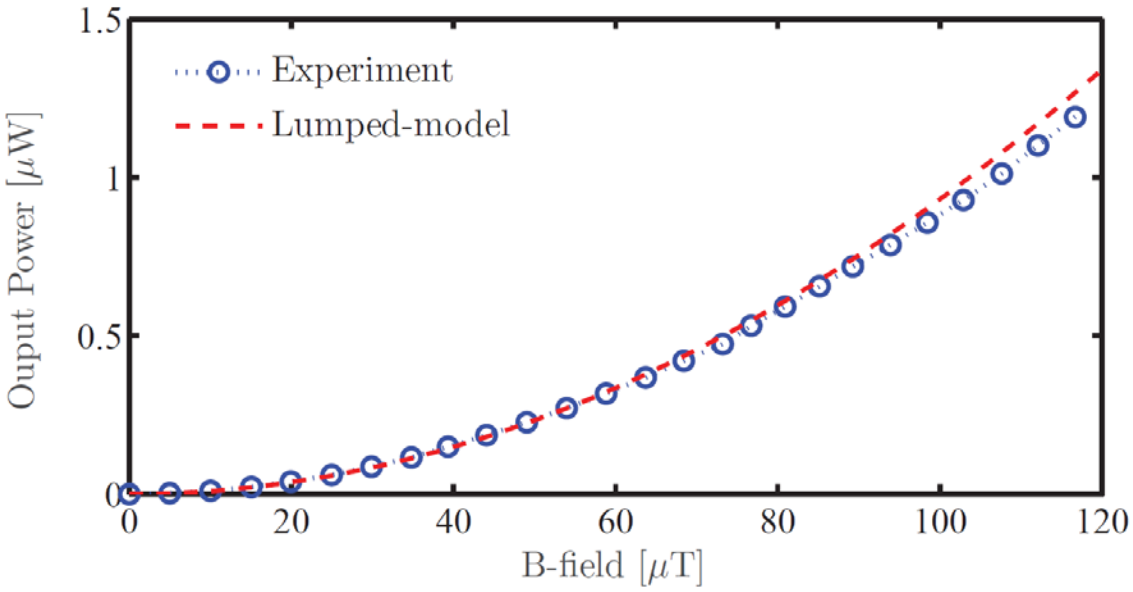

Figure 4.15: Experimental and modeled MME transducer power output under varying B-field at 350 Hz operating frequency. Figure reproduced with permission from Binh Duc Truong and Dr. Shad Roundy [47].

CHAPTER 5

COMPARATIVE ANALYSIS OF TRANSDUCER TYPES

Having established confidence in the analytical models describing MME and ME transducer performance, a constrained nonlinear optimization algorithm was used to compare transducer designs. In particular this was to be done by constraining the optimization based on the constraints associated with operating and constructing IMD devices.

5.1 Optimization Algorithm

The algorithm settled upon was a commonly used interior point algorithm known as “fmincon” which is a function built into MATLAB, a numerical computing software. Although the explicit workings of the fmincon function are proprietary, the function is described as a gradient-based optimization method that is best suited for use with objective functions that are continuous and have continuous derivatives[54]. This algorithm was chosen given that the functions that predict the power output of the two presented transducer designs met this continuity criteria.

In terms of operation, the solver takes an objective function, $f(\boldsymbol{x})$, upper and lower bounds for inputs, $\boldsymbol{x}$, an initial guess, $\boldsymbol{x}_0$ and iterates to find a minimizer of $\boldsymbol{x}$ subject to linear and nonlinear constraints. For extensive information on the workings of this function see [54], [55].

5.2 Optimization Constraints and Bounds

To ensure that the models were being compared under the same circumstances, constraints were chosen to be used on all optimization runs regardless of transducer design or material composition. The first constraints dealt with the application limitations of the device, such as the maximum device volume, chosen to be $2mm^3$. Although somewhat arbitrary, this number matches the approximate desirable size for an IMD power source.

The next constraint was that of the applied magnetic field strength for operating the transducers. Although much higher-level fields can physically be produced, there are limitations to what magnitudes humans can be safely subjected. Efforts have gone into characterizing what is known as the maximum permissible exposure (MPE) for magnetic flux density and multiple safety standards have subsequently been published. For this work two, common standards were chosen to bound the optimization. The first is the Institute of Electrical and Electronics Engineers' (IEEE) standard on magnetic MPE of the head and torso under controlled environment conditions[56], [57]. The second is the International Commission on Non-Ionizing Radiation Protection's (ICNIRP) standard on maximum occupational exposure to magnetic fields[58].

Under both standards the allowable MPE varies by frequency as is shown in Figure 5.1. By examination, it is apparent that the ICNIRP standard is generally more conservative than the IEEE standard, which will be shown to have a large effect on transducer performance.

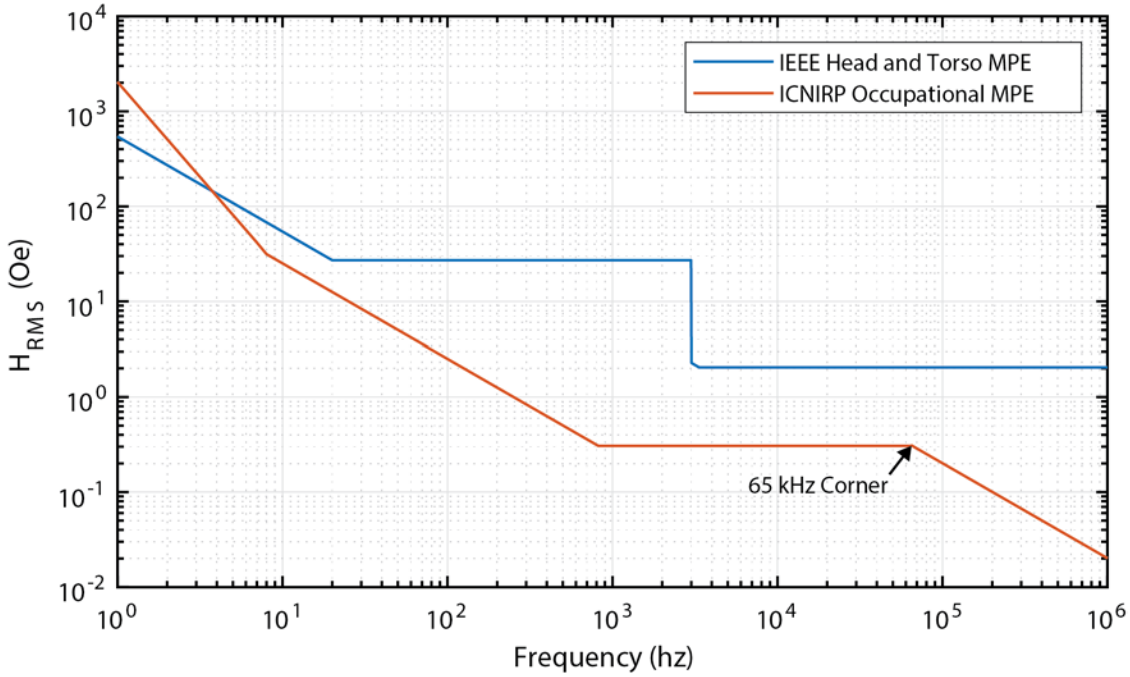

Figure 5.1: Magnetic MPE levels for IEEE and ICNIRP Standards. Adapted from [56]–[58].

In addition to the volume and field constraints set by the IMD application of the transducers, constraints and boundaries had to be set to ensure realistic manufacturable optimization results. The chosen approach was to use aspect ratio constraints rather than absolute upper bounds for almost all the optimization variables. First, aspect ratios of 200:1 were set for the length l_0 and width w to the total structure thickness, t_t, (magnet thickness excluded). Additionally, the aspect ratio of the length to width ($l_0 : w$) was set to a minimum of 0.1:1 and a maximum of 10:1.

It should be noted that in both the aspect ratio width refers to the entire structure width. However, the aspect ratio's length, l_0 does not refer to the total structure length, but the length from both transducers' center anchors to the free edges. This means for the ME transducer $l_0 = .5 * l$ and for the MME transducer $l_0 = L$.

Like the maximum volume, these values are again somewhat arbitrary and would in actuality vary based on exact fabrication methods. However, they do serve, as will be shown by the optimization results, to keep the devices to dimensions that could conceivable be built by microfabrication techniques. In addition to the aspect ratios, a lower bound was set for the piezoelectric thickness at 10 μm with all of the other parameters' lower bounds being set at or near zero. The 10 μm number was chosen based on the difficulties associated with manufacturing thin PZT. In this case the assumption was made that the layer would be manufactured by bonding bulk PZT to a substrate then polishing it down to the desired height. Hypothetically this method should work well at any height but in practice, thicknesses below 10 μm are hard to achieve. The upper bounds of the algorithm were all set at arbitrarily high values and were only decreased to aid the solver in converging faster, in hopes they would not actually bound the optimization results. In addition to these universally applicable constraints, design specific constraints also had to be set.

5.2.1 ME Transducer Optimization Constraints

For the ME device, only one additional constraint was added which is based on an assumption made by the Dong et al. model. In particular, the model makes the assumption that the extensional strain is uniformly transferred from the MS material through the thickness of PE material. This assumption is most valid where the laminate length is much longer than its thickness. As the laminate length begins to approach the magnitude of the thickness, the strain gradient becomes less and less uniform. This is due to the bowing of the free faces normal to the length of the laminate which fundamentally reduces the actual normal strain transferred between to the two layers. This effect is

demonstrated in Figure 5.2 where the normal strain gradient of the right-hand side of an ME transducer is shown via a finite element model (FEM). Visible in this figure is the bowing and non-uniform strain at the free face.

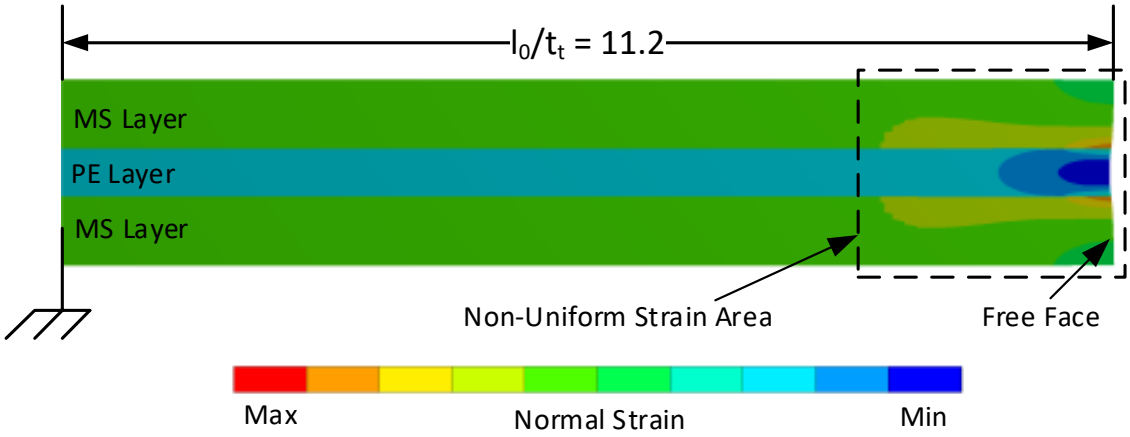

Figure 5.2: Normal strain gradients for right hand side of an ME device.

The plot in Figure 5.3 was generated by varying the length to width ratio (l_0/t_t) in the FEM and comparing the resulting average strain to the perfect strain assumption. The figure indicates that as l_0/t_t increases, the perfect strain assumption becomes more valid. However, as the ratio decreases into the single digits and below the model assumption rapidly begins to deteriorate. This indicates that the Dong et al. model would over predict power delivery for structures with l_0/t_t ratios below 10:1. To prevent this overprediction, the lower bound for the l_0/t_t ratio was set to be 10:1.

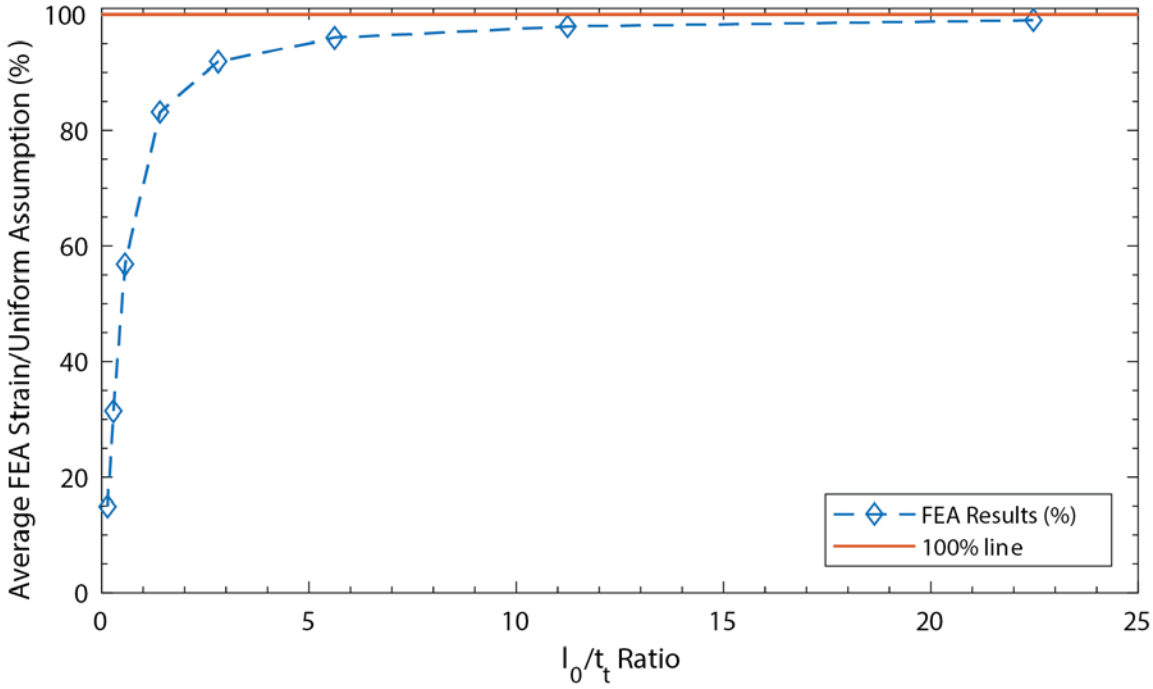

Figure 5.3: Average FEM strain, normalized by perfect the strain assumption, vs l_0/t_t ratio.

5.2.2 MME Transducer Optimization Constraints

The MME transducer, like the ME transducer, required a limitation corresponding to the assumptions made by the model. As was discussed in section 3.2.2 a value of 1:4 was chosen as the minimum L_m: l_0 ratio. Also, the PE beam substrate thickness, t_s was set to zero to yield optimization results that would be a theoretical upper bound for power delivery. If t_s is left unconstrained, the optimization would result in $t_s = 0$. Although this is difficult to manufacture in practice, it does provide the upper bound on power generation. This choice leaves the substrate geometry and material to be decided based on the constraints of microfabrication process. Finally, an upper bound on the magnet height or thickness (h) was imposed to ensure realistic geometries for the magnet. This variable, as will be shown, was varied iteratively until the final optimization result was realistic.

5.3 ME Optimization and Results

For the ME optimization, six variables were required to be varied while power delivery was optimized: The transducer length (l), width (w), PE thickness (t_p), MS thickness (t_m) loaded natural frequency (ω), and finally load resistance (R_l). Two material configurations were optimized, Galfenol-PZT and Metglas-PZT, using the material properties shown in Tables 4.3 and 4.4. The mechanical quality factor was chosen to be 48, from the average of the results witnessed during the transducer experiments. As subsets to the configurations, each was optimized under three different magnetic field constraints, the ICNIRP and IEEE safety standards, and a baseline magnetic field input of 1 Oe peak at any frequency. The results of the optimization are seen in Table 5.1.

By examination it is evident that Metglas-PZT configuration outperforms the Galfenol-PZT configuration. Additionally, under 1 Oe or the IEEE standards both configurations push to a short wide structure (see Figure 5.3), maximizing the allowable $l_0 : t_t$ ratios, minimizing the $l_0 : w$ ratio, and raising the operating frequency to MHz levels. The configurations subject to ICNIRP standard have an opposite effect going towards a long, skinny, and thin structure maximizing the PE thickness and the $l : w$ ratio while maximizing the $l_0 : t_t$. In all cases the optimization maximized the allotted volume of 2mm^3.

Using 100 μW as the threshold of minimum power delivery to allow an IMD to function, it is evident that the two optimized material configurations are only viable under

the IEEE standard. If held to the ICNIRP standard, an ME device would not be an adequate design under a 2mm^3 volume constraint.

Table 5.1: ME optimization results.

Optimized Parameter	**Galfenol-PZT configuration**			**Metglas-PZT**		
	1 Oe	**ICNIRP**	**IEEE**	**1 Oe**	**ICNIRP**	**IEEE**
l (total)	2 mm	21.5 mm	2 mm	2 mm	25.2 mm	2 mm
l_0	1 mm	10.8 mm	1 mm	1 mm	12.6 mm	1 mm
w	10.0 mm	1.1 mm	10.0 mm	10.0 mm	1.26 mm	10.0 mm
t_p	19.4 μm	15.9 μm	19.4 μm	25.5 μm	18.1 μm	25.5 μm
t_m	40.3 μm	33.5 μm	40.3 μm	37.3 μm	22.4 μm	37.3 μm
ω_1	697.6 kHz	65.0 kHz	697.6 kHz	914.7 kHz	71.9 kHz	914.7 kHz
R_l	16.5 Ω	117.1 Ω	16.5 Ω	16.6 Ω	93.4 Ω	16.6 Ω
$\boldsymbol{P_{avg}}$	**.89 mW**	**15.6 μW**	**7.4 mW**	**5.1 mW**	**62.6 μW**	**42.7 mW**
H_p	1.0 Oe	0.44 Oe	2.89 Oe	1.0 Oe	.40 Oe	2.89 Oe
Volume	2.0 mm^3	2.0 mm^3	2.0 mm^3	2.0 mm^3	2.0 mm^3	2.0 mm^3
n	.81	0.81	.81	.75	.71	.75
$l_0 : t_t$	10:1	129:1	10:1	10:1	200:1	10:1
$w : t_t$	100:1	14:1	100:1	100:1	20:1	100:1
$l_0 : w$	0.1:1	9.6:1	0.1:1	0.1:1	10:1	0.1:1
σ_T	.107 MPa	.048 MPa	.309 MPa	.196 MPa	.074 MPa	.567 MPa

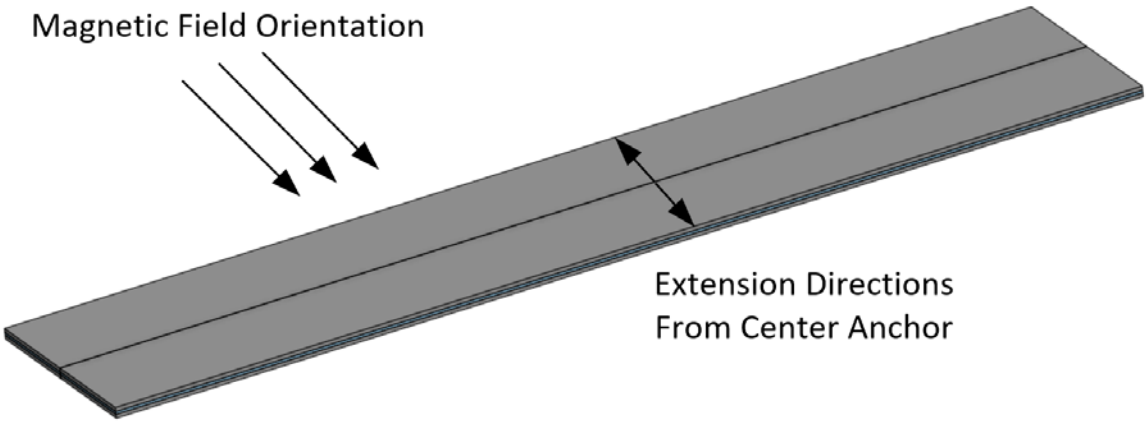

Figure 5.4: CAD representation optimized Metglas-PZT device under IEEE safety conditions. Anchor plane shown as centerline.

5.3.1 Discussion of ME Optimization Results

To show that the results of the optimizer were both realistic and useful it is important to discuss and justify some of the results. First note that the whole numbers for the resulting geometry were simply artifacts of the whole numbers used in the constraint ratios and were not unexpected. Next, to explain the difference in the geometric results between IEEE and ICNIRP standards, the situations must be examined individually.

As has been stated, IEEE device led to a short wide and thick structures operating 697.6 kHz and 914.7 kHz. For these values the magnetic field amplitude allowed by the IEEE standard is shown to be locally constant, but for a given field magnitude the energy contained within a field increases with frequency. This indicates that to maximize power output under the IEEE condition, the natural frequency, ω_1 of the structure should also be maximized.

It is well known that the natural frequency of a structure scales proportionally with the structure's stiffness and is inversely proportional to its mass. Under the constrained volume the mass of the structure is generally constant, leaving the frequency to be

adjusted primarily by changing the structure's stiffness. By using Hooke's Law extensional stiffness of a beam (or laminate) can be shown to be proportional to the cross-sectional area of the beam divided by its length. Thus, if the desire is to maximize stiffness, and subsequently ω_1 and the power delivered, the optimization should result in the short, wide, and thick structure seen in the optimization. If left unconstrained, the optimization would tend toward an infeasible structure with an infinite stiffness. These conclusions also match that of the 1 Oe field case where the field level was also constant across frequency.

For the ICNIRP device geometry the optimization converged on long, narrow and thin devices operating at 65 kHz and 71.9 kHz which seems to defy the logic presented for the IEEE case. However, the same logic can be applied to justify this result as well. The ICNIRP standard, unlike the IEEE standard, shows a linear decline of allowable field strength in the 65 kHz to 10 MHz frequency range. Because of the attenuation of field strength, it is obvious that the optimization clearly worked to reduce ω_1 to reach the 65 kHz corner. This would indicate that ICNIRP standard's local attenuation overwhelms the increase in energy density due to the increase in operating frequency.

With greater power delivery levels now to be obtained at lower operating frequencies, the same logic applied to the IEEE works to explain the ICNIRP results. To reduce ω_1 the optimizer now worked to decrease stiffness by making structures that are as long, narrow, and thin as the constraints permitted, essentially yielding the opposite geometry of the IEEE result.

In examining these geometric results, the question was posed whether the resulting devices were strong enough to handle the forces induced by the optimized structures or if

they would fracture before delivering any power. To check this, the maximum tensile stress, σ_T, was calculated for all of the optimal cases. The worst stress case matched that of the highest power delivery case, the IEEE Metglas-PZT configuration. At about .567 MPa, σ_T was about two orders of magnitude less than PZT-5A's tensile strength of about 50-70 MPa[59]. This indicates that all of the structure designs generated by the optimization would be very unlikely to fracture during normal operation.

A final point of discussion concerns which magnetostrictive material is most effective. Although both MS materials under the IEEE standard yield structures which greatly exceed the 100 μW threshold, Metglas tends to have a higher MS coefficient and is stiffer than Galfenol. This difference allows for greater device extension and a thicker piezoelectric layer relative to the magnetostrictive layer thickness. Based on the optimization, these differences equate to a Metglas device being able to deliver about six times more power than a comparable Galfenol device. This result, taken with the knowledge that Metglas typically requires a much lower bias field strength than Galfenol, makes it clear that Metglas is the MS material of choice for an ME transducer being used to power IMDs.

5.4 MME Optimization and Results

The MME optimization only required the use of five variables all related to the geometry of the transducer: the beam length, or half the transducer length (L), the beam width (w), the piezo electric thickness (t_p), the magnet length L_m, and the magnet height (h). The optimal power output (P_{avg}), operating frequency (ω_1), and load resistance (R_l) were all calculated with closed form equations.

Only one material configuration was optimized with PZT-5A and Neodymium 52 being used for the PE and magnet materials respectively. The material properties found in Table 4.3 were used to represent the PZT and the properties used for the Neodymium are shown in Table 5.2. Like the ME transducer, the configuration was optimized under the three magnetic field conditions, 1 Oe peak, ICNIRP and IEEE. Finally, the mechanical quality factor was set equal to 42 based on the results from Truong and Roundy.

Table 5.2: Neodymium 52 material properties [60].

Property	**Value**
Remnant Magnetic Polarization, J_r	1.46 T
Magnet Density, ρ_M	7500 kg/m^3

Unlike the ME optimization, the MME optimization required some iteration to yield a manufacturable result. This was largely due to not knowing what a suitable upper bound for the magnetic height would be. Initially a 10 mm height was set as the upper bound to satisfy the solver inputs but not actually bound the height. Despite this large upper bound, the results rapidly maximized the magnet height under each of the magnetic field scenarios, even with other geometric parameters varying between the ICNIRP and IEEE standards. The results of the optimizations done under this constraint are shown in Table 5.3.

Examination showed that the geometries were infeasible for manufacture because they called for a magnet that was about 50 times thicker than its length and 500 times thicker than the PE beam to which it was to be attached. Additionally, under the IEEE field standard, the predicted maximum bending stress, σ_B, exceeded PZT-5A's bending

strength of 140.4 MPa by over 40%. This indicated that if the structure could be built it would fracture during operation [61].

Subsequently, the upper bound for the magnet height was reduced to 5 mm and the optimization algorithm was run again. The corresponding results are also shown in Table 5.3. As before, the algorithm maximized the height of the magnet up to the imposed bound, but the results were still ultimately infeasible with the magnet still being too thick to be integrated with the rest of the structure. Additionally, under the IEEE condition the bending stress still exceeded the fracture strength of the beam.

Table 5.3: MME optimization results for 10 mm and 5 mm magnet.

Optimized Parameter	**PZT Bimorph Configuration Max h = 10 mm**			**PZT Bimorph Configuration Max h = 5 mm**		
	1 Oe	**ICNIRP**	**IEEE**	**1 Oe**	**ICNIRP**	**IEEE**
$2L$	1.63 mm	8.00 mm	1.63 mm	3.11 mm	8.00 mm	3.11 mm
L, l_0	0.82 mm	4.00 mm	0.82 mm	1.56mm	4.00 mm	1.56 mm
w	0.49 mm	0.40 mm	0.49 mm	0.51 mm	0.40 mm	0.51 mm
t_p	10.0 µm	10.0 µm	10.0 µm	10.0 µm	10.0 µm	10.0 µm
L_m	0.21 mm	0.24 mm	0.21 mm	0.39 mm	0.48 mm	0.389mm
h	10.0 mm	10.0 mm	10.0 mm	5.0 mm	5.0 mm	5.0 mm
ω_1	831 Hz	61 Hz	831 Hz	325 Hz	61 Hz	325 Hz
R_l	2.34 MΩ	8.9 MΩ	2.34 MΩ	3.0 MΩ	8.2 MΩ	3.0 MΩ
$\boldsymbol{P_{avg}}$	**8.4 µW**	**130 µW**	**12.4 mW**	**5.9 µW**	**120 µW**	**8.7 mW**
H_p	1 Oe	5.82 Oe	38.39 Oe	1 Oe	5.56 Oe	38.39 Oe
Volume	2.0 mm^3	2.0 mm^3	2.0 mm^3	2.0 mm^3	2.0 mm^3	2.0 mm^3
$L_m : l_0$	4:1	16.5:1	4:1	4:1	8.1:1	4:1
$l_0 : t_t$	41:1	200:1	41:1	78:1	200:1	78:1
$w : t_t$	24:1	20:1	24:1	25:1	20:1	25:1
$l_0 : w$	1.7:1	10:1	1.7:1	3:1	10:1	3:1
σ_B	5.3 MPa	37 MPa	205 MPa	5.1 MPa	37 MPa	195 MPa

Finally, the upper bound for the optimization was reduced once more to 1 mm which yielded the results seen in Table 5.4. As before, the magnet height was maximized by the solver. Unlike the previous cases, the resulting geometry (which was the same for all field cases which will be discussed in detail later) was in the realm of feasibility. In particular this geometry was much more manufacturable given that the magnet was almost a perfect cube with all sides being equal or close to the width of the beam. A CAD representation of this geometry is shown in Figure 5.5.

Table 5.4: Final MME optimization results.

Optimized Parameter	**PZT Bimorph Configuration**		
	1 Oe	**ICNIRP**	**IEEE**
$2L$ (total length)	8.0 mm	8.0 mm	8.0 mm
L, l_0	4.0 mm	4.0 mm	4.0 mm
w	0.93 mm	0.93 mm	0.93 mm
t_p	10.0 μm	10.0 μm	10.0 μm
L_m	1.0 mm	1.0 mm	1.0 mm
h	1.0 mm	1.0 mm	1.0 mm
ω_1	109 Hz	109 Hz	109 Hz
R_l	1.9 MΩ	8.2 MΩ	1.9 MΩ
$\boldsymbol{P_{avg}}$	**2.7 μW**	**26 μW**	**3.6 mW**
H_p	1 Oe	5.56 Oe	38.39 Oe
Volume	2.0 mm^3	2.0 mm^3	2.0 mm^3
L_m: l_0	4:1	4:1	4:1
l_0: t_t	200:1	200:1	200:1
w: t_t	46:1	46:1	46:1
l_0: w	4.3:1	4.3:1	4.3:1
σ_B	2.6 MPa	8.5 MPa	100 MPa

In terms of power output, like the ME transducer, the IEEE condition yielded mW power levels, exceeding the 100 μW threshold while the ICNIRP condition did not. Given that under this constraint the IEEE condition exceeded the desired power output, had bending stress less than the fracture strength, and yielded a result that conceivably could be manufactured, this result was sufficient for comparing to the ME optimization results.

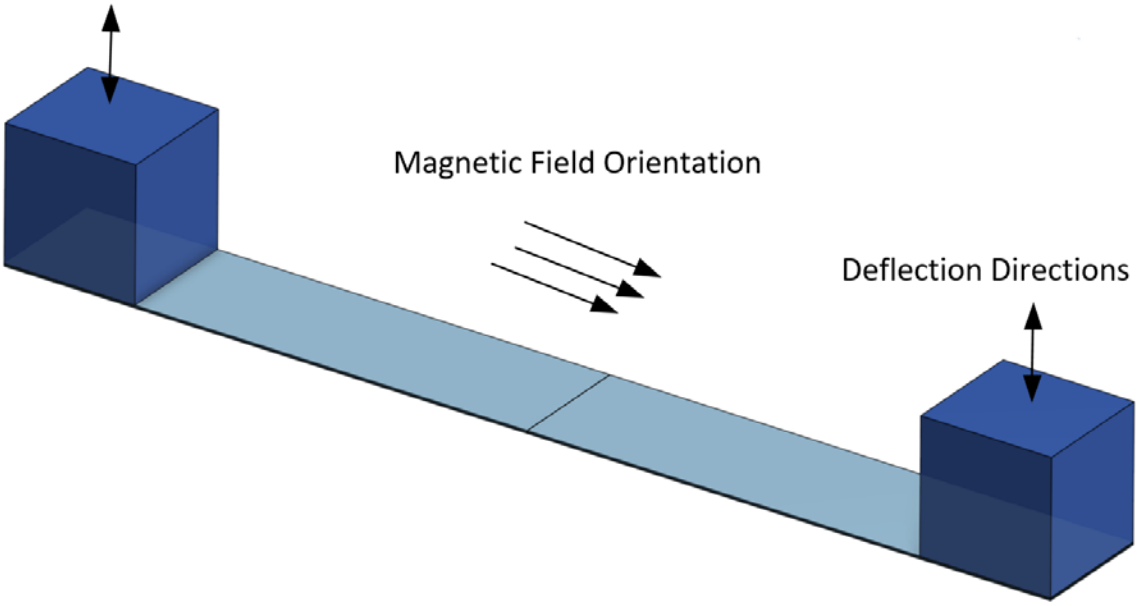

Figure 5.5: CAD representation optimized PZT-Brass-N52 device constrained to 1 mm magnet height. Anchor plane shown as centerline.

5.4.1 Discussion of MME Optimization Results

Because the MME transducer optimizations required some iteration, insight can be gained about the optimization's process and the subsequent optimal geometry. The optimization consistently settled on the thinnest possible PE beam and attempted to maximize the magnet size and in so doing increased the moment applied to the beam. This would indicate that optimization was maximizing the force induced onto the beam from moment of the permanent magnet. This was to be expected given that model indicates that power output should scale directly with force applied (see equation 3.20).

In addition to minimizing the PE thickness and maximizing the magnet thickness, the structure also increased the power delivery by adjusting the natural frequency of the device. Like the ME device before, the IEEE standard was locally constant in the area of this optimization. Table 5.3 shows that both the 10 mm and 5mm IEEE optimizations stiffened the device by making wider and shorter cantilever beams moving the devices

toward more energy dense operating frequencies. Alternatively, the ICNIRP standard was locally decreasing the allowable magnetic field with increasing frequency in the area of MME optimization. Subsequently Table 5.3 also shows that the optimizations worked to reduce the loaded natural frequency of the ICNIRP device by making a long, narrow cantilever. This phenomenon is fundamentally the same as that witnessed during the ME device optimizations.

These frequency results wouldn't be visible, however, if the magnet height was initially bounded to 1 mm because under this bound the optimization led to the exact same loaded natural frequency and subsequent geometry under all magnetic field cases. This indicated that by bounding the magnet to 1 mm the geometry was so constrained that it essentially limited the solver to one particular natural frequency. Being skeptical of this result, the optimization was rerun and found that indeed the ICNIRP and IEEE standard yielded the same geometry for the 1 mm constraint up until the allowable magnet height exceeded about 2 mm.

Despite being comfortable with the reality of results of the MME device, the implications of the optimizations are somewhat concerning. In particular, under the best power delivery case the magnetic field had a very large magnitude of over 38 Oe which even at low frequencies would be difficult to generate. Additionally, the magnitude of the operating stress is close enough to the fracture strength that the fatigue life of the device might be very short. Finally, this optimization is a best-case scenario for power delivery and manufacturing, in that a center substrate should likely be added to lower the bending stress in the PE and generally make the device more durable. Such an addition would intrinsically reduce the power delivery and make fabrication even more difficult, given how long and thin the piezoelectric layers would be.

5.5 Comparison of Optimized Structures

The average power outputs and operating frequencies for each of the optimized structures are summarized in Table 5.4. It is visible that the ME transducer delivers about 2 to 12 times the power of the MME under IEEE conditions depending on the material configuration. Under the ICNIRP conditions the MME device delivers about two thirds more power than the Galfenol ME device but delivers under half that of the Metglas ME device. It is also shown that for either transducer design the IEEE limitation allows for three orders of magnitude more power delivered than that of the ICNIRP standard for the ME devices and 3-4 orders for the MME device. This highlights that under the 100 μW threshold only the IEEE field standard allows for enough power delivery in a constrained volume 2 mm^3. Under this threshold it also evident that the ME laminate design is the preferred design for powering IMDs.

In addition to the power delivery, Table 5.4 also brings to light that the AC field magnitudes are an order of magnitude larger for the MME transducer design despite ultimately delivering less power than the alternative. Finally, it also shows that ME transducers operate at frequencies in the 10s of kHz to single MHz where the MME transducers function near 100 Hz.

Table 5.5: Power outputs of MME and ME transducers compared.

Field Level	**ME (Galfenol-PZT)**	**ME (Metglas-PZT)**	**MME (PZT-N52)**
1 Oe Peak	0.89 mW at 697.6 kHz (H_p = 1 Oe)	5.1 mW at 914.7 kHz (H_p = 1 Oe)	2.7 µW at 109 Hz (H_p = 1 Oe)
ICNIRP	15.6 µW at 65.0 kHz (H_p = .44 Oe)	62.6 µW at 71.9 kHz (H_p =.40 Oe)	26.0 µW at 109 Hz (H_p = 2.0 Oe)
IEEE	7.4 mW at 697.6 kHz (H_p = 2.89 Oe)	42.7 mW at 914.7 kHz (H_p = 2.89 Oe)	3.6 mW at 109 Hz (H_p = 38.4 Oe)

CHAPTER 6

FUTURE WORK AND CONCLUSIONS

This work constitutes a review of ME and MME transducer designs and compares them for potential use as wireless power receivers for IMDs. This was done by augmenting and experimentally validating an existing ME laminate model, incorporating a tandem MME modeling effort and combining the resulting models to perform a constrained numerical optimization. The conclusions that can be drawn from this effort as well as possible future work are discussed in the following sections.

6.1 Conclusions

By looking purely at useful amounts power delivered, the magnetoelectric laminate appears to be the more viable candidate for wirelessly powering a microscale IMD. However, deeper examination tells a more intricate story. Although a somewhat simple first order optimization, the results make clear that the extensional mode of the ME transducer allows for a significant amount of power delivery at the cost of having to operate at MHz frequencies which might be less desirable depending on which medical standard is being used. Conversely the MME bending design operates at lower frequencies where the magnet field is less susceptible to tissue absorption but ultimately delivers about a tenth of the power. This observation, and the results of the optimization, lead one to believe that the bending mode might be preferable to extension. However, in

terms of power delivery and stress to the structure, massive magnetostrictive materials seem to be a better method of magneto-mechanical coupling than that of the moment induced by a permanent magnet. Unfortunately, this work only compares the full magnetoelectric performance of two transducer design and does not compare the efficiency of the two methods of magnetic to mechanical domain transduction. In order to definitively decide which is generally the most effective, not just when applied to IMD applications, additional work should be done to normalize and compare permanent magnet performance to that of magnetostrictive material.

Another important take away deals with the standard to which the transducers are held. Clearly the IEEE standard is far less conservative than ICNIRP in that IEEE generally allows for milliwatts of power where ICNIRP allows for microwatts. If medically safe, the IEEE standard gives potential for either design to be conceivably implemented. If held to the ICNIRP standard none of the devices could provide enough power to run an IMD given that requires 100 μW.

The experiments also showed that the changes made to the Dong et al. model can be used to predict power output of ME laminates. It can also be concluded from both the experiments and the optimization that Metglas is a superior choice to Galfenol for MME transducers, particularly those constrained to the IEEE and ICNIRP standards. Because these standards prevent either Metglas or Galfenol from ever reaching saturation strain, the driving factor becomes the rate of magnetostriction and not the absolute amount of magnetostriction. Under the allowed field bandwidths this rate is much larger for Metglas than for Galfenol. Additionally, as was witnessed by the results of the experimental validation, the high permeability of Metglas makes it far easier to magnetically bias than Galfenol. Finally, although not within the scope of this research, the fact that Metglas'

amorphous nature makes the magnetostriction occur anywhere in a plane as opposed to Galfenol, which is limited to a single axis, makes Metglas a better candidate for solving the likely alignment issues between the field and transducer.

6.2 Future Work

Based on the knowledge gained from this research, a tremendous amount of work remains to be done to move towards the goal of powering an IMD with an oscillating magnetic field. In particular, it seems prudent that future work would further investigate and incorporate MS material biasing into lumped models, investigate alternative MS-PE coupled geometries, and finally attempt to build a microscale Metglas-PZT transducer.

The need to better understand the required biasing for a given geometry was made apparent by the mismatch in model and experimental values of the Galfenol-PZT device. In particular it would be wise to investigate if the optimal bias field changes based on the change in impedance of the transducer circuit, and how that subsequently effects the magnetostrictive coefficient.

The need to examine different transducer geometries comes from the fact that there is a large range of operating frequencies in which neither the ME nor the MME device seems to perform well. The simplest geometry that might bridge this gap would be that of the ME unimorph which operates in bending, unlike the ME bimorph which operates in extension. This transducer design is not new; research has gone into adding center substrates to unimorphs to tune and lower their operating frequency, however these additions make the transducer more difficult to model and have not been examined from a power delivery perspective[62]. Furthermore, other, more exotic, geometries would be

valuable if they were designed to utilize Metglas' planar magnetostrictive property and minimize sender-receiver misalignment issues.

Finally, the purpose of this research was to provide a viable design foundation for a micro-fabricated magnetic power receiver. With this design foundation in place, work can now move forward with manufacturing and characterization. In particular, the results of the IEEE Metglas-PZT magnetoelectric laminate optimization reveal such an opportunity. Although not trivial, manufacture should lead to a viable method for wirelessly powering IMDs.

REFERENCES

[1] T. Battelino and M. Phillip, “Effect of continuous glucose monitoring on hypoglycemia in type 1 diabetes,” *Diabetes …*, vol. 34, no. 4, pp. 795–800, 2011.

[2] S. Vaddiraju, “Technologies for Continuous Glucose Monitoring: Current Problems and Future Promises,” *J Diabetes Sci Technol*, vol. 4, no. 6, pp. 1540–1562, 2010.

[3] D. Seo, J. M. Carmena, J. M. Rabaey, E. Alon, and M. M. Maharbiz, “Neural Dust: An Ultrasonic, Low Power Solution for Chronic Brain-Machine Interfaces,” *arXiv Prepr. arXiv*, pp. 1307–2196, 2013.

[4] A. Arsiwala, P. Desai, and V. Patravale, “Recent advances in micro/nanoscale biomedical implants,” *J. Control. Release*, vol. 189, no. 2014, pp. 25–45, 2014.

[5] R. R. Harrison *et al.*, “A low-power integrated circuit for a wireless 100-electrode neural recording system,” *IEEE J. Solid-State Circuits*, vol. 42, no. 1, pp. 123–133, 2007.

[6] S. H. Song, A. Kim, S. Member, B. Ziaie, and S. Member, “Omni - Directional Ultrasonic Powering for Millimeter - Scale Implantable Devices,” vol. 62, no. 11, pp. 1–8, 2015.

[7] A. Denisov and E. Yeatman, “Ultrasonic vs. Inductive Power Delivery for Miniature Biomedical Implants,” in *2010 International Conference on Body Sensor Networks*, 2010, pp. 84–89.

[8] N. Tesla, “System of transmission of electrical energy.,” 645,576, 1900.

[9] N. Tesla, “The transmission of electrical energy without wires as a means for furthering peace,” *Elect. World Eng.*, pp. 21–24, 1905.

[10] S. Y. R. Hui, Z. Wenxing, and C. K. Lee, “A critical review of recent progress in mid-range wireless power transfer,” *IEEE Trans. Power Electron.*, vol. 29, no. 9, pp. 4500–4511, 2014.

[11] R. C. O’Handley, J. K. Huang, D. C. Bono, and J. Simon, “Improved Wireless, Transcutaneous Power Transmission for In Vivo Applications,” *IEEE Sens. J.*, vol. 8, no. 1, pp. 57–62, 2008.

[12] H. Basaeri, D. B. Christensen, and S. Roundy, “A Review of Acoustic Power

Transfer for Bio-Medical Implants," *Smart Mater. Struct.*, vol. 25, no. 12, p. 123001, 2016.

[13] P. Abiri *et al.*, "Inductively powered wireless pacing via a miniature pacemaker and remote stimulation control system," *Sci. Rep.*, vol. 7, no. 1, pp. 1–10, 2017.

[14] A. Ben Amar, A. B. Kouki, and H. Cao, "Power approaches for implantable medical devices," *Sensors (Switzerland)*, vol. 15, no. 11, pp. 28889–28914, 2015.

[15] L. Radziemski and I. R. S. Makin, "In vivo demonstration of ultrasound power delivery to charge implanted medical devices via acute and survival porcine studies," *Ultrasonics*, vol. 64, pp. 1–9, 2016.

[16] Y. Rajavi, M. Taghivand, K. Aggarwal, A. Ma, and A. S. Y. Poon, "An RF-powered FDD radio for neural microimplants," *IEEE J. Solid-State Circuits*, vol. 52, no. 5, pp. 1221–1229, 2017.

[17] M. Fiebig, "Revival of the magnetoelectric effect," *J. Phys. D. Appl. Phys.*, vol. 38, no. 8, 2005.

[18] W. C. Röntgen, "Ueber die durch Bewegung eines im homogenen electrischen Felde befindlichen Dielectricums hervorgerufene electrodynamische Kraft," *Ann. Phys.*, vol. 271, no. 10, pp. 264–270, 1888.

[19] I. E. Dzyaloshinskii, "On the magneto-electrical effect in antiferromagnets," *J. Sov. Phys.*, vol. 10, no. 3, pp. 628–629, 1960.

[20] B. D. H. Tellegen, "The gyrator, a new electric network element," *Phillips Res. Reports*, vol. 3, pp. 81–101, 1948.

[21] C. W. Nan, "Magnetoelectric effect in composites of piezoelectric and piezomagnetic phases," *Phys. Rev. B*, vol. 50, no. 9, pp. 6082–6088, 1994.

[22] K. H. Shin, M. Inoue, and K. I. Arai, "Preparation and properties of elastically coupled electro-magnetic elements with a bonding structure," *IEEE Trans. Magn.*, vol. 34, no. 4 PART 1, pp. 1324–1326, 1998.

[23] J. Ryu, A. V Carazo, K. Uchino, and H.-E. Kim, "Magnetoelectric Properties in Piezoelectric and Magnetostrictive Laminate Composites," *Jpn. J. Appl. Phys.*, vol. 40, pp. 4948–4951, 2001.

[24] I. D. Mayergoyz, *Handbook of giant magnetostrictive materials*. Elsevier, 1999.

[25] D. M. J., D. Zhangxiang, C. F. T., and F. A. B., "Magnetostrictive Devices," *Wiley Encyclopedia of Electrical and Electronics Engineering*. 27-Dec-1999.

[26] "Scientists spy Galfenol's inner beauty mark," *phys.org*, 2009. [Online]. Available: https://phys.org/news/2009-03-scientists-spy-galfenol-beauty.html.

[Accessed: 01-Apr-2018].

[27] R. A. Kellog, “Development and modeling of iron-gallium alloys,” Iowa State University, 2003.

[28] Metglas Inc, “Data Sheet: Metglas 2605,” *2605SA1 Data Sheet*. 2011.

[29] J. Zhai, S. Dong, Z. Xing, J. Li, and D. Viehland, “Giant magnetoelectric effect in Metglas/polyvinylidene-fluoride laminates,” *Appl. Phys. Lett.*, vol. 89, no. 8, pp. 1–4, 2006.

[30] J. Zhai, Z. Xing, S. Dong, J. Li, and D. Viehland, “Magnetoelectric laminate composites: An overview,” *J. Am. Ceram. Soc.*, vol. 91, no. 2, pp. 351–358, 2008.

[31] S. Dong, J. Cheng, J. F. Li, and D. Viehland, “Enhanced magnetoelectric effects in laminate composites of Terfenol-D/Pb(Zr,Ti)O 3 under resonant drive,” *Appl. Phys. Lett.*, vol. 83, no. 23, pp. 4812–4814, 2003.

[32] S. Dong, J. F. Li, and D. Viehland, “Characterization of magnetoelectric laminate composites operated in longitudinal-transverse and transverse-transverse modes,” *J. Appl. Phys.*, vol. 95, no. 5, pp. 2625–2630, 2004.

[33] S. Dong, J. F. Li, and D. Viehland, “Longitudinal and transverse magnetoelectric voltage coefficients of magnetostrictive/piezoelectric laminate composite: Theory,” *IEEE Trans. Ultrason. Ferroelectr. Freq. Control*, vol. 50, no. 10, pp. 1253–1261, 2003.

[34] S. Dong, J. F. Li, and D. Viehland, “Longitudinal and transverse magnetoelectric voltage coeffcients of magnetostrictive/ piezoelectric laminate composite: experiments,” *IEEE Trans. Ultrason. Ferroelectr. Freq. Control*, vol. 51, no. 7, pp. 794–799, 2004.

[35] S. Priya and D. J. Inman, *Energy Harvesting Technologies*. Springer US, 2008.

[36] I. Paprotny, Q. Xu, W. W. Chan, R. M. White, and P. K. Wright, “Electromechanical energy scavenging from current-carrying conductors,” *IEEE Sens. J.*, vol. 13, no. 1, pp. 190–201, 2013.

[37] J. Han, J. Hu, Z. Wang, S. X. Wang, and J. He, “Enhanced performance of magnetoelectric energy harvester based on compound magnetic coupling effect,” *J. Appl. Phys.*, vol. 117, no. 14, 2015.

[38] R. Jahns, R. Knoechel, and E. Quandt, “Method for measuring a magnetic field using magnetoelectric sensors,” 05-Jul-2016.

[39] S. Marauska, R. Jahns, H. Greve, E. Quandt, R. Kn, and B. Wagner, “MEMS magnetic field sensor based on magnetoelectric composites,” *Micromechanics and Microengineering*, vol. 22, 2012.

[40] S. Marauska *et al.*, “Highly sensitive wafer-level packaged MEMS magnetic field sensor based on magnetoelectric composites,” *Sensors Actuators A Phys.*, vol. 189, pp. 321–327, 2013.

[41] T. Nan, Y. Hui, M. Rinaldi, and N. X. Sun, “Self-biased 215MHz magnetoelectric NEMS resonator for ultra-sensitive DC magnetic field detection,” *Sci. Rep.*, vol. 3, p. 1985, 2013.

[42] C. W. Nan, M. I. Bichurin, S. Dong, D. Viehland, and G. Srinivasan, “Multiferroic magnetoelectric composites: Historical perspective, status, and future directions,” *J. Appl. Phys.*, vol. 103, no. 3, 2008.

[43] M. Paluszek *et al.*, “Magnetoelectric composites for medical application,” in *Composite Magnetoelectrics*, Elsevier, 2015, pp. 297–327.

[44] G. Yang, H. Talleb, A. Gensbittel, and Z. Ren, “FEM Modeling of a Magnetoelectric Transducer for Autonomous Micro Sensors in Medical Application,” *Sens. Imaging*, vol. 16, no. 1, pp. 1–10, 2015.

[45] C. Shuo, C. Clemens, and A. D. P., “Electrodynamic Vibrational Energy Harvesting,” in *Micro Energy Harvesting*, 1st ed., D. Briand, E. M. Yeatman, and S. Roundy, Eds. 2015, pp. 175–197.

[46] Y. Zhou, S. Chul Yang, D. J. Apo, D. Maurya, and S. Priya, “Tunable self-biased magnetoelectric response in homogenous laminates,” *Appl. Phys. Lett.*, vol. 101, no. 23, 2012.

[47] B. D. Truong and S. Roundy, “Model Validation and Investigation on the Efficiency of Wireless Power Transfer System with Middle Clamped Piezoelectric Reciever,” *unpublished*.

[48] J. J. Abbott, “Parametric design of tri-axial nested Helmholtz coils,” *Rev. Sci. Instrum.*, vol. 86, no. 5, pp. 1–10, 2015.

[49] L. Bian, Y. Wen, P. Li, Q. Gao, and M. Zheng, “Magnetoelectric transducer with high quality factor for wireless power receiving,” *Sensors Actuators, A Phys.*, vol. 150, no. 2, pp. 207–211, 2009.

[50] *PSI-5A4E Piezoceramic Plates and Sheets*. Woburn: Systems, Piezo, 2011.

[51] E. Summers, “Galfenol – a New Class of Magnetostrictive Materials.”

[52] Measurement Specialties, *Piezo Film Sensors Technical Manual*, no. March. 2006.

[53] E. Freeman *et al.*, “Improving the magnetoelectric performance of Metglas/PZT laminates by annealing in a magnetic field,” *Smart Mater. Struct.*, vol. 26, no. 8, p. 85038, 2017.

[54] MathWorks, “fmincon,” 2018. [Online]. Available: https://www.mathworks.com/help/optim/ug/fmincon.html#busp5fq-6. [Accessed: 11-May-2018].

[55] MathWork, “Constrained Nonlinear Optimization Algorithms,” 2018. [Online]. Available: https://www.mathworks.com/help/optim/ug/constrained-nonlinear-optimization-algorithms.html#brnox01. [Accessed: 11-May-2018].

[56] IEEE International Committee on Electromagnetic Safety, *IEEE Standard for Safety Levels With Respect to Human Exposure to Radio Frequency Electromagnetic Fields, 3 kHz to 300 GHz*. New York, NY: The Institute of Electrical and Electronics Engineers, Inc., 2006.

[57] IEEE Standards Coordinating Committee, *IEEE Standard for Safety Levels with Respect to Human Exposure to Electromagnetic Fields, 0–3 kHz*. New York, NY: The Institute of Electrical and Electronics Engineers, Inc., 2003.

[58] International Commission on Non-Ionizing Radiaton Protection, “ICNIRP Guidelines for Limiting Exposure To Time-Varying Electric, Magnetic, and Electromagnetic Fields (up to 300 GHz),” *Health Phys.*, vol. 74, no. (4), p. 494-522;, 1998.

[59] X. Kornmann and C. Huber, “Microstructure and mechanical properties of PZT fibres,” *J. Eur. Ceram. Soc.*, vol. 24, no. 7, pp. 1987–1991, 2004.

[60] K&J Magnetics, “Specification.” [Online]. Available: https://www.kjmagnetics.com/specs.asp. [Accessed: 05-May-2018].

[61] S. R. Anton, A. Erturk, and D. J. Inman, “Bending strength of piezoelectric ceramics and single crystals for multifunctional load-bearing applications,” *IEEE Trans. Ultrason. Ferroelectr. Freq. Control*, vol. 59, no. 6, pp. 1085–1092, 2012.

[62] Z. Xing, S. Dong, J. Zhai, L. Yan, J. Li, and D. Viehland, “Resonant bending mode of Terfenol-D⁄steel⁄Pb(Zr,Ti)O3 magnetoelectric laminate composites,” *Appl. Phys. Lett.*, vol. 89, no. 11, p. 112911, 2006.